

Molecular clouds under the FUV feedback: factories of CO-dark gas

Mutsuko Inoguchi¹★, Takashi Hosokawa², Shin Mineshige¹, and Jeong-Gyu Kim³

¹*Department of Astronomy, Kyoto University, Sakyo-ku, Kyoto 606-8502, Japan*

²*Department of Physics, Kyoto University, Sakyo-ku, Kyoto 606-8502, Japan*

³*Department of Astrophysical Sciences, Princeton University, Princeton, NJ 08544, USA*

Accepted XXX. Received YYY; in original form ZZZ

ABSTRACT

The star formation in molecular clouds is inefficient. The ionizing EUV radiation ($h\nu \geq 13.6$ eV) from young clusters has been considered as a primary feedback effect to limit the star formation efficiency (SFE). We here focus on effects of the stellar FUV radiation ($6 \text{ eV} \leq h\nu \leq 13.6$ eV) during the cloud disruption stage. The FUV radiation may further reduce the SFE via photoelectric heating, and it also affects the chemical states of the gas that is not converted to stars (“cloud remnants”) via photodissociation of molecules. We have developed a one-dimensional semi-analytic model which follows the evolution of both the thermal and chemical structure of a photodissociation region (PDR) during the dynamical expansion of an HII region. We investigate how the FUV feedback limits the SFE, supposing that the star formation is quenched in the PDR where the temperature is above a threshold value (e.g., 100K). Our model predicts that the FUV feedback contributes to reduce the SFEs for the massive ($M_{\text{cl}} \gtrsim 10^5 M_{\odot}$) clouds with the low surface densities ($\Sigma_{\text{cl}} \lesssim 100 M_{\odot} \text{pc}^{-2}$). Moreover, we show that a large part of the H₂ molecular gas contained in the cloud remnants should be “CO-dark” under the FUV feedback for a wide range of cloud properties. Therefore, the dispersed molecular clouds are potential factories of the CO-dark gas, which returns into the cycle of the interstellar medium.

Key words: stars: formation – HII regions – photodissociation region (PDR)

1 INTRODUCTION

The evolution of galaxies is closely related to the star formation activities. In nearby galaxies, the overall star formation rate is quite low; the cold molecular gas is converted to stars in a slow pace. The resulting depletion timescale of the molecular gas is \sim Gyr over the galactic scale (e.g., Kennicutt & Evans 2012). By contrast, the star formation occurs in the much shorter timescale over the small ($\lesssim 100$ pc) cloud scales (e.g. Lee et al. 2016). The lifetime of an individual giant molecular cloud (GMC) is estimated to be less than ~ 10 Myr (e.g., Fukui & Kawamura 2010). A possible explanation for the above observations is that only a small fraction of the gas is used to form stars in each cloud. Physical processes responsible for such a low star formation efficiency (SFE) are yet to be fully clarified.

A promising process to limit the SFE is the so-called “stellar feedback”, i.e., radiative and kinetic energy injection from stars into natal clouds (e.g. Dale 2015; Naab & Ostriker 2017; Krumholz et al. 2018). The SFEs are lowered

if the clouds are promptly destroyed by the feedback before a large part of the gas turns into stars. Recent studies show that such an evolution is caused indeed by the feedback from high-mass stars in GMCs (e.g., Kruijssen et al. 2019). It is further suggested that the cloud destruction advances over only a few Myrs, which is shorter than the stellar lifetime. Therefore, radiation-driven or wind-driven bubbles expanding around high-mass stars before the first supernova explosion are necessary to be considered primarily.

H II regions created by the stellar ionizing (EUV; $h\nu \geq 13.6$ eV) radiation cause the dynamical bubble expansion in GMCs (e.g., Yorke 1986). Since the expansion speed is supersonic with respect to the surrounding cold medium, the H II bubble expands driving a preceding shock front. The shocked gas is taken into a shell around the H II region, which continues to expand sweeping up the surrounding medium into the shell. While the gas dynamics varies depending on density structure of the clouds (e.g., Franco et al. 1990), theoretical studies have suggested that the resulting EUV feedback operates to limit the SFE (e.g. Whitworth 1979; Williams & McKee 1997; Matzner 2002; Kim et al. 2016). In recent years, a number of authors have

★ Contact e-mail: mutsuko@kustastro.kyoto-u.ac.jp

conducted radiation-hydrodynamics numerical simulations that directly follow the EUV feedback in GMCs that are filled with turbulence in reality (e.g., Mellema et al. 2006; Vázquez-Semadeni et al. 2010; Dale et al. 2012; Geen et al. 2015; Howard et al. 2016; Gavagnin et al. 2017; Kim et al. 2018; Haid et al. 2019; He et al. 2019). Overall, these studies have confirmed that the EUV feedback lowers the SFEs, though its impact depends on cloud properties such as the mass and surface density.

There are extensive studies regarding the ionizing radiation feedback that have been performed. In fact, however, the dissociating radiation (FUV; $6.0 \text{ eV} \leq h\nu \leq 13.6 \text{ eV}$) as well as ionizing radiation is emitted from young star clusters. Many studies have investigated the dynamical effect of the radiation pressure of the FUV radiation. Indeed, some of them shows that the feedback caused by the radiation force contributes to regulating the star formation in GMCs, although the resulting SFE is a bit higher than what observations suggest (e.g., Thompson & Krumholz 2016; Raskutti et al. 2016, 2017; Kim et al. 2018).

Whereas the radiation pressure force is one dynamical aspect of the FUV feedback, we in this paper consider the other aspect of the thermal and chemical FUV feedback on GMCs. Hereafter we use the terms of the EUV feedback and FUV feedback to designate the dynamical effects caused by H II regions and thermal and chemical effects caused by PDRs, respectively. The FUV radiation creates a photodissociation region (PDRs), where the gas is heated up via photoelectric effect, around an H II region (e.g., Hollenbach & Tielens 1999). The local Jeans mass is enhanced by such additional heating, which prevents the gravitational collapse of dense cores. As a result, the FUV radiation may further contribute to the reduction of the SFEs in GMCs (e.g., Roger & Dewdney 1992; Diaz-Miller et al. 1998; Inutsuka et al. 2015). For example, Forbes et al. (2016) shows that the photoelectric heating plays the dominant role on determining the star formation rate in dwarf galaxies ($\sim \text{kpc-scale}$) rather than other feedback effects (but see also Hu et al. 2017). In the same vein, Peters et al. (2017) and Butler et al. (2017) have incorporated the FUV feedback in simulations following the star formation in a $\sim \text{kpc-scale}$ region of the Galactic disk, concluding that it is necessary to explain the observed depletion timescale of $\sim \text{Gyr}$. On the individual GMC scale ($\lesssim 100 \text{ pc}$), by contrast, the effects of FUV feedback has not been fully investigated yet.

The low SFE means that most of the GMC gas is returned into the cycle of the interstellar medium, without being turned into stars. A part of such a "remnant" gas may be recycled for the subsequent GMC formation. The stellar FUV radiation also substantially affects the physical and chemical states of the cloud remnants. Since the FUV radiation destroys molecules via photodissociation, it generally creates cold H_2 gas associated with little amount of CO molecules (e.g., van Dishoeck & Black 1988; Wolfire et al. 2010). Since such gas is difficult to be observed via CO emission, it is called as "CO dark". Recent observations via γ -ray (Grenier et al. 2005), dust continuum (Planck Collaboration et al. 2011), and C^+ line emission (Pineda et al. 2013, 2014) suggest the existence of the CO-dark gas, and no less than $\sim 30 - 70 \%$ of the molecular gas is actually CO dark in our Galaxy. Theoretical studies also support such Galactic-scale observations (e.g. Smith et al. 2014; Gong et al. 2018). On

the cloud scale, the appearance of the CO-dark gas during the formation of molecular clouds has been suggested (e.g., Clark et al. 2012). However, the CO-dark gas phase while the clouds are being dispersed is yet to be further studied (e.g., Hosokawa & Inutsuka 2007; Seifried et al. 2019).

As seen above the stellar FUV radiation should cause the additional feedback that affects the SFEs and chemical compositions of the cloud remnants. Whereas fully considering such effects requires expensive numerical simulations of radiation-magneto-hydrodynamics, we here adopt a one-dimensional semi-analytic treatment that guides our understanding. Kim et al. (2016) have developed a semi-analytic model for expansion of an H II region driven by photoionization and radiation pressure. The minimum SFEs limited by the EUV feedback have been evaluated as functions of the cloud masses and surface densities. However, they ignore the roles of the FUV feedback. Hence we construct a new model based on Kim et al. (2016), where both the FUV and EUV feedback effects are included. In order to evaluate the FUV feedback, we solve the thermal and chemical structure of PDRs around H II regions assuming the spherical symmetry. Although simple, this approach allows us to consider impacts of the FUV feedback against a variety of GMCs having different properties. We first investigate how much the FUV feedback contributes to reducing the SFEs. Next we consider the chemical compositions of the GMC remnants under the FUV feedback, showing that they are potential factories of the CO-dark molecular gas.

The rest of the paper is organized as follows. We present our models in Section 2, where we outline the overall methodology in Section 2.1 and describe how to couple the dynamics and the thermal and chemical processes operating in the PDR in Sections 2.2 and 2.3. In Section 3 we show our main results. First we present a representative case of the time evolution of the thermal and chemical structure in the PDR in Section 3.1. Then we study the effects of the FUV feedback on limiting the SFE in Section 3.2, and possible chemical compositions of the cloud remnants in Section 3.3. We provide the relevant discussion and conclusion in Sections 4 and 5.

2 MODEL

2.1 Methodology

We first describe our model in this section. We consider spherical and uniform density clouds which are characterized by the mass M_{cl} and surface density Σ_{cl} . The cloud radius R_{cl} and hydrogen number density n_0 are related to M_{cl} and Σ_{cl} as

$$R_{\text{cl}} = \sqrt{M_{\text{cl}}/\pi\Sigma_{\text{cl}}} \quad (1)$$

$$\begin{aligned} n_0 &= \frac{M_{\text{cl}}}{\frac{4}{3}\pi R_{\text{cl}}^3 \mu_{\text{H}}} \\ &= \frac{3}{4\mu_{\text{H}}} M_{\text{cl}}^{-1/2} \Sigma_{\text{cl}}^{3/2}, \end{aligned} \quad (2)$$

where $\mu_{\text{H}} = 1.4m_{\text{H}}$ is the mean molecular weight per hydrogen nuclei. We consider clouds with $M_{\text{cl}} = 10^4, 10^5, 10^6 M_{\odot}$ below. The surface density is varied so that the resulting number density should fall on a typical range of observed

Table 1. Parameter set

$M_{\text{cl}} (M_{\odot})$	$\Sigma_{\text{cl}} (M_{\odot}/\text{pc}^2)$	$R_{\text{cl}} (\text{pc})$	$n (\text{cm}^{-3})$
10^4	15 – 700	13.2 – 1.94	30 – 10000
10^5	31 – 1506	31.9 – 4.60	30 – 10000
10^6	67 – 3246	68.7 – 9.90	30 – 10000

molecular clouds, $30 \text{ cm}^{-3} < n_0 < 10^4 \text{ cm}^{-3}$ (e.g. Tan et al. 2014). Table 1 summarizes the ranges of the parameter values we consider.

Our aim is to derive minimum SFE required for cloud disruption ε_{min} as functions of the cloud mass M_{cl} and surface density Σ_{cl} . We here focus on the FUV feedback to limit the SFE. For a given set of $(M_{\text{cl}}, \Sigma_{\text{cl}})$, we start our calculation by putting a star cluster with the mass of $M_* = \varepsilon M_{\text{cl}}$ at the origin. Here we first take a trial value for the SFE ε . We envision that an H II region and surrounding photodissociation region (PDR) created by the stellar EUV and FUV radiation expands around the central cluster in the cloud. Following Kim et al. (2016), we calculate the EUV photon number luminosity as

$$S_{\text{EUV}} = \Xi_{\text{EUV}} M_*, \quad (3)$$

where the ratio of the stellar mass to the EUV luminosity Ξ_{EUV} is calculated with the SLUG code (Krumholz et al. 2015). Similarly, we calculate the FUV photon number luminosity

$$S_{\text{FUV}} = \Xi_{\text{FUV}} M_*, \quad (4)$$

where we again use the SLUG code to evaluate Ξ_{FUV} (see Appendix A for details). We assume that Ξ is time-independent. This is a reasonable approximation, since the dynamical timescale $t_{R_{\text{cl}}}$ is shorter than the lifetimes of massive main-sequence stars. The dynamics of the expanding H II region and surrounding shell can be described by the analytic formula (see Section 2.2). The effects of the FUV radiation on the thermal and chemical structure outside the H II region are then calculated (Section 2.3).

These calculations are performed using the arbitrary choice of ε , and we determine the minimum SFE by the following iterative procedure. If ε first assumed is too small, only a small central part of the cloud is affected by the cluster radiation. The further star formation is possible for such a case, meaning that the minimum SFE should be higher. We repeat the calculations with increasing ε incrementally. If ε becomes sufficiently large, the radiative feedback influences the whole natal cloud leaving no room for the further star formation. We assume that the minimum SFE ε_{min} is determined for such a case (section 2.4). The obtained value of ε_{min} depends on the feedback effects considered. The FUV feedback potentially reduces the SFE in addition to the EUV feedback because it heats the gas outside the H II region to hinder the star formation. The above procedure is basically the same as in Kim et al. (2016), except that we additionally consider the stellar FUV radiation.

2.2 Dynamics of expanding H II regions

We here model the dynamical expansion of an H II region created around the cluster in the natal molecular cloud. In what follows we assume that the photoionized gas has the

constant temperature $T_{\text{H II}} = 10^4 \text{ K}$ for simplicity. The initial size of an H II region is determined by the so-called Strömgen radius

$$r_{\text{IF},0} = \left(\frac{3S_{\text{EUV}} f_{\text{ion}}}{4\pi n_0 (1-\varepsilon)^2 \alpha_{\text{B}}} \right)^{1/3}, \quad (5)$$

where $\alpha_{\text{B}} = 2.59 \times 10^{-13} (T_{\text{H II}}/10^4 \text{ K})^{-0.7}$ is the case B recombination coefficient (Osterbrock 1989), and $f_{\text{ion}} = 0.73$ denotes the fraction of the EUV photons absorbed by the gas (not by the dust, Krumholz & Matzner 2009). We note that f_{ion} varies with the product $S_{\text{EUV}} n_{\text{H II}}$ (Draine 2011), although the thermal pressure force and the H II region size only weakly depend on f_{ion} as $r_{\text{IF}} \propto f_{\text{ion}}^{1/3}$ and $F_{\text{thm}} \propto f_{\text{ion}}^{1/2}$ (Kim et al. 2016).

Because the internal thermal pressure is much higher than that in the ambient medium, the H II region starts to expand. As considered in Kim et al. (2016), however, the dynamics of the H II region is generally affected by additional effects such as the radiation pressure exerted on the photoionized gas (e.g., Draine 2011) and swept-up shell (e.g., Krumholz & Matzner 2009; Ishiki & Okamoto 2017). However, we omit such additional effects for simplicity. Recent theoretical studies show that the radiation pressure effect is particularly important for disrupting GMCs with high surface densities $\Sigma_{\text{cl}} \gtrsim 100 M_{\odot} \text{pc}^{-2}$ (e.g., Murray et al. 2010; Fall et al. 2010). We separately examine its effects on our results in Section 4.3.

Once the H II region begins to expand, the ambient gas is swept up to be retained in a shell. The shell is bounded by the ionization front and preceding shock front. The shell mass M_{sh} is estimated as

$$M_{\text{sh}} = \frac{4}{3} \pi r_{\text{IF}}^3 \rho_0 (1-\varepsilon) - M_{\text{H II}}. \quad (6)$$

Here, r_{IF} is the radial position of the ionization front, $M_{\text{H II}}$ is the mass of ionized gas,

$$M_{\text{H II}} \approx \frac{4\pi}{3} r_{\text{IF}}^3 \mu_{\text{H}} n_{\text{H II}}, \quad (7)$$

where the number density of ionized gas $n_{\text{H II}}$ varies with ionization front radius as $n_{\text{H II}} \propto r_{\text{IF}}^{-3/2}$. The expansion law, or the time evolution of r_{IF} , is derived with the equation of motion of the shell,

$$\frac{d}{dt} (M_{\text{sh}} v_{\text{sh}}) = F_{\text{out}} - F_{\text{in}}, \quad (8)$$

where $v_{\text{sh}} = dr_{\text{sh}}/dt$ is the shock velocity, F_{out} and F_{in} represent the forces exerted on the outer and inner surface of the shell. As noted above, we only consider the thermal pressure of the ionized gas as the outward force F_{out} ,

$$F_{\text{thm}} = 4\pi r_{\text{IF}}^2 \cdot 2n_{\text{H II}} k_{\text{B}} T_{\text{H II}}, \quad (9)$$

which scales as $F_{\text{thm}} \propto n_{\text{H II}} r_{\text{IF}}^2 \propto r_{\text{IF}}^{1/2}$. We ignore F_{in} for simplicity. Equation (8) is solved analytically, and we obtain

$$r_{\text{IF}}(t) = r_{\text{IF},0} \left(1 + \frac{7}{4} \sqrt{\frac{4}{3}} \frac{c_s t}{r_{\text{IF},0}} \right)^{4/7}, \quad (10)$$

where $c_s = \sqrt{2k_{\text{B}} T_{\text{H II}} / \mu_{\text{H}}}$ is the sound speed in H II region (Hosokawa & Inutsuka 2006). Equation (10) differs from the

well-known expansion law given by Spitzer (1978) by the factor of $\sqrt{4/3}$, but it actually provides the better approximation as proven by radiation-hydrodynamics numerical simulations (e.g., Bisbas et al. 2015; Kim et al. 2017). Note that equation (10) is basically the same as that given by Kim et al. (2016) but we only consider the thermal pressure of the photoionized gas.

2.3 Thermal and chemical structure of photodissociation regions

For every snapshot of an expanding H II region within the cloud, we calculate the thermal and chemical structure in the surrounding photodissociation region (PDR). Below we consider the following seven chemical species of e^- , H^+ , H^0 , H_2 , C^+ , O^0 and CO. We assume the total abundance of C and O atoms as $x_C = 3.0 \times 10^{-4}$ and $x_O = 4.6 \times 10^{-4}$ (Wolfire et al. 1995), where x denotes the number fraction relative to the hydrogen nuclei.

2.3.1 One-zone thermal and chemical equilibrium model

We make use of the one-zone modeling of the thermal and chemical equilibrium state of the interstellar medium (e.g., Wolfire et al. 1995; Koyama & Inutsuka 2000). Consider the gas with a given density n exposed by a FUV radiation field with G_0 . We determine the unknown variables, the gas temperature T and chemical number fractions x_{H^+} , x_{H_2} , x_{CO} , by solving the following equations

$$\frac{de}{dt} = \Gamma(n, T, x^*) - \Lambda(n, T, x^*) \quad (11)$$

$$\frac{dx_{H^+}}{dt} = R_{H^+}^{\text{form}}(n, T, x^*) - R_{H^+}^{\text{rec}}(n, T, x^*) \quad (12)$$

$$\frac{dx_{H_2}}{dt} = R_{H_2}^{\text{form}}(n, T, x^*) - R_{H_2}^{\text{dis}}(n, T, x^*) \quad (13)$$

$$\frac{dx_{CO}}{dt} = R_{CO}^{\text{form}}(n, T, x^*) - R_{CO}^{\text{dis}}(n, T, x^*) \quad (14)$$

where e is internal energy of the gas, Γ and Λ are the heating and cooling rates, and x^* represents $(x_{H^+}, x_{H_2}, x_{CO})$. In the present study, we only consider C^+ and CO as carbon compounds and thus set $x_{C^+} = x_C - x_{CO}$.

A full list of thermal and chemical processes associated with the terms on the R.H.S of equations (11) - (14) is presented in Table 2. We here only briefly describe some of them. Those readers who are interested in more details may refer to the references therein. As the heating processes, we incorporate the photoelectric emission from grains and H_2 dissociation by the FUV radiation, ionization by the background soft X-ray radiation, and H_2 formation releasing the binding energy. The radiative cooling is primarily caused via the line emission of [C II], [O I], Ly- α , and CO. We assume the optically-thin limit for these line emission. It is equivalent to ignoring the trapping effect, for which possible effects on our conclusions are discussed in Section 4.2. To avoid overcooling, we set the minimum gas temperature to be 8 K. Regarding the formation of CO molecules, we adopt the simple method given by Nelson & Langer (1997), where CO molecules are approximately formed from C^+ ions and O atoms. Gong et al. (2018) pointed out that the Nelson & Langer (1999) chemical network significantly underestimates CO abundance for $n \lesssim 500 \text{ cm}^{-3}$ and $A_V < 5$. However, we

use the chemical network by Nelson & Langer in the present study, since we focus on the CO abundance at dense shell where $n > 10^4 \text{ cm}^{-3}$. We also assume the constant dust temperature $T_d = 8 \text{ K}$ for the all cases considered. The dust temperature is used to estimate the reformation rate of H_2 molecules and the thermal gas-dust coupling rate via collisions. We also investigate the effects of varying T_d in our calculations in Section 4.2.

2.3.2 Time-evolution of multi-zone structure

We calculate the spatial variation of the thermal and chemical state in the PDR around an H II region by repeating the one-zone calculations as follows. At a given time $t = t_j$, the radius and mass of the shell, $M_{\text{sh}}(t_j)$ and $r_{\text{sh}}(t_j)$, are described by equations (6) and (10). By setting radial grids, we discretize the outer PDR including the shell into cells with the column density $\Delta N_H \sim 10^{19} \text{ cm}^{-2}$ per each. The number of the grids is typically ~ 1000 . The distance from the ionization front to the i -th grid r_i is

$$r_i = r_{\text{IF}}(t_j) + \sum_{k=0}^i \Delta N_H / n_k, \quad (15)$$

which corresponds to the dust optical depth in the outward direction

$$\tau_{\text{in}, i} = \sigma_d \sum_{k=0}^i \Delta N_H, \quad (16)$$

and the dust optical depth from the edge of the cloud $\tau_{\text{out}, i}$

$$\tau_{\text{out}, i} = \sigma_d \sum_{k=i}^N \Delta N_H, \quad (17)$$

The normalized FUV flux at $r = r_i$ is written as

$$G_i = \frac{1}{F_H} \frac{S_{\text{FUV}}}{4\pi r_i^2} \exp(-\tau_{\text{in}, i}) + G_{\text{bg}} \exp(-\tau_{\text{out}, i}), \quad (18)$$

where N is the total number of the grids, $\sigma_d = 10^{-21} \text{ cm}^2 \text{H}^{-1}$ is the absorption cross section by dust grains per hydrogen nucleus, and $F_H = 1.21 \times 10^7 \text{ cm}^{-2} \text{s}^{-1}$ is the normalization factor which represents the background field near the Solar system (the so-called Habing unit, i.e., Habing 1968; Draine & Bertoldi 1996). The last term of the unity in equation (18) represents this background exactly. The mass summation over the cells located at $r \leq r_i$ is

$$M_i = \sum_{k=0}^i 4\pi r_k^2 \mu_H \Delta N_H. \quad (19)$$

By comparing M_i to the total shell mass M_{sh} , we judge whether the i -th cell is still within the shell or not. As far as $M_i < M_{\text{sh}}$, the cell is regarded as a part of the shell. We determine the thermal and chemical states of such cells in an iterative manner as follows. We assume that the gas pressure within the shell is equal to that of the H II region, $P_{\text{th}} = 2n_{\text{HII}}k_B T_{\text{HII}}$. So we initially provide the pressure instead of the density in a one-zone calculation, unlike in Section 2.3.1. With the given pressure P_{th} and FUV field G_i , we calculate the unknown variable (T_i, x_i^*) by solving equations (11)-(14) so that the resulting pressure $P_{\text{sh}} = n_i(1 + x_{e^-} - x_{H_2}/2)k_B T_i$ matches P_{th} . By doing that, we

Table 2. The thermal and chemical processes included in our model

	Processes	Reference
Heating $\Gamma(n, T, x^*)$	photoelectric heating	1
	ionization by soft X-ray	2
	H ₂ photodissociation	3
	H ₂ formation	3
	Cooling $\Lambda(n, T, x^*)$	fine structure line emission
	[C II] 158 μm	3
	[O I] 63 μm , 44.2 μm , 145.6 μm	3
	Ly α line emission	4
	CO rotational line emission	5
	collision with dust grains	6
$R_{\text{form}}^{\text{H}^+}(n, T, x^*)$	ionization by soft X-ray	2
$R_{\text{rec}}^{\text{H}^+}(n, T, x^*)$	case B recombination	7
$R_{\text{form}}^{\text{H}_2}(n, T, x^*)$	dust catalysis	8
	associative detachment	3
$R_{\text{dis}}^{\text{H}_2}(n, T, x^*)$	photodissociation	8,9
	dust collision	8
$R_{\text{form}}^{\text{CO}}(n, T, x^*)$	CO formation	10, 11
$R_{\text{dis}}^{\text{CO}}(n, T, x^*)$	photodissociation	10, 11

References: (1) Bakes & Tielens (1994); (2) Wolfire et al. (1995); (3) Hollenbach & McKee (1979); (4) Spitzer (1978); (5) McKee et al. (1982); (6) Hollenbach & McKee (1989); (7) Osterbrock (1989); (8) Tielens & Hollenbach (1985); (9) Draine & Bertoldi (1996); (10) Langer (1976); (11) Nelson & Langer (1997)

also determine the number density n_i as well as (T_i, x_i^*) . Once (n_i, T_i, x_i^*) are fixed, we then move on to the next $(i + 1)$ -th cell and repeat the same procedures. If M_i exceeds M_{sh} , the following cells are considered to be outside of the shell as the un-shocked ambient gas. We take exactly the same method as in Section 2.3.1 for such cells; we calculate (T_i, x_i^*) for the given number density $n_0(1 - \varepsilon)$ and FUV field G_i . We continue the calculations until reaching the cloud edge, i.e., for $M_i < M_{\text{gas}} = M_{\text{cl}}(1 - \varepsilon) - M_{\text{H II}}$.

2.4 Cloud disruption criteria

To determine the minimum SFE of the cloud, we need some criteria of the cloud disruption as in Kim et al. (2016). We investigate the effects of the FUV feedback on top of the EUV feedback previously studied. So we first use the exactly the same criterion as in Kim et al. (2016):

Criterion 1 (EUV feedback): An H II region and shell are assumed to expand as far as the shell velocity v_{sh} is larger than the critical velocity $v_{\text{bind}} = \sqrt{GM_{\text{cl}}(1 + \varepsilon)/R_{\text{cl}}}$,

$$v_{\text{bind}} \approx 5 \text{ km/s} \left(\frac{M_{\text{cl}}}{10^5 M_{\odot}} \right)^{1/4} \left(\frac{\Sigma_{\text{cl}}}{100 M_{\odot} \text{pc}^{-2}} \right)^{1/4} (1 + \varepsilon)^{1/2}. \quad (20)$$

If the trial value of ε is too small, the expansion stalls well before the shell reaches the cloud edge. We iteratively increase ε until $v_{\text{sh}} = v_{\text{bind}}$ is satisfied at the cloud edge, i.e., $r = R_{\text{cl}}$. This gives the minimum SFE.

Note that the above is not the only criterion investigated in Kim et al. (2016). They have also adopted other criteria, showing that the obtained minimum SFE does not largely change. Since our aim is to study the effects of the FUV radiation, we only focus on one representative case.

Criterion 2 (FUV feedback): We assume that the

star formation is suppressed in a warm PDR, where the gas temperature is above the threshold value 100 K. The minimum SFE is determined by the FUV feedback when the gas at the cloud edge is heated above 100 K before engulfed by the expanding shell.

Although the temperature is raised to $\sim 100 - 1000$ K in the PDR, the corresponding sound speed is much smaller than that of the photoionized gas. Therefore, as often presumed, the resulting FUV feedback should be weaker than the EUV feedback. The FUV effects would not operate to disrupt the entire structure of the molecular clouds. We rather suppose that the star formation in the PDR is locally hindered with the lack of the cold (~ 10 K) materials. Since the exact strength of the FUV feedback is uncertain, we also consider Criterion 1 for limiting the SFEs. We only estimate effects of the FUV feedback on the chemical compositions of cloud remnants for such cases.

3 RESULTS

3.1 Time evolution of thermal and chemical structure

First we present typical evolution of the thermal and chemical structure in the PDR around an H II region. Here we spotlight one particular case with the molecular cloud mass $M_{\text{cl}} = 10^4 M_{\odot}$ and surface density $\Sigma_{\text{cl}} = 300 M_{\odot} \text{pc}^{-2}$. We follow the evolution with a star cluster with $M_* = \varepsilon_{\text{min}} M_{\text{cl}} \approx 1220 M_{\odot}$ formed at the cloud center¹. The corresponding stellar EUV and FUV photon number luminosities are

¹ For this representative case, we find that the minimum SFE $\varepsilon \approx 0.12$ is insensitive to the choice of cloud disruption criteria (see also Section 3.2).

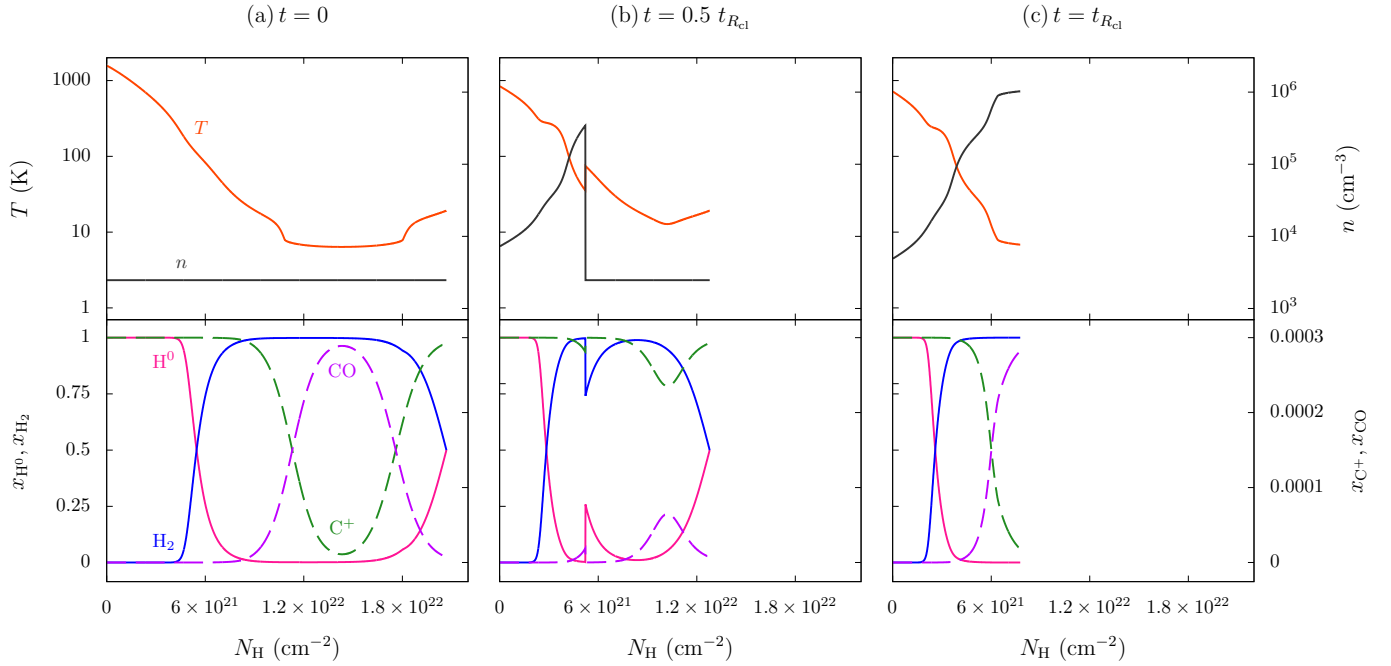


Figure 1. Time evolution of the thermal and chemical structure in the photodissociation region around an H II region. The cloud mass and surface density are $M_{\text{cl}} = 10^4 M_{\odot}$ and $\Sigma_{\text{cl}} = 300 M_{\odot} \text{pc}^{-2}$ for this case. The panels (a), (b), and (c) show the snapshots at the different epochs of (a) $t = 0$, (b) $t = 0.5 t_{R_{\text{cl}}}$ and (c) $t = t_{R_{\text{cl}}}$, where $t_{R_{\text{cl}}}$ is the time when the shell reaches the cloud edge. The horizontal axis denotes the column density of hydrogen nuclei measured from the ionization front. *Top:* Plotted are the gas temperature (red line) and density (gray line), for which the scaling is presented with the left- and right-hand axis. *Bottom:* Plotted are the fractional abundances of H I (red solid line), H₂ (blue solid line), C II (green dashed line), and CO (purple dashed line). The left-hand (right-hand) axis is used for scaling of H I and H₂ (C II and CO) abundances.

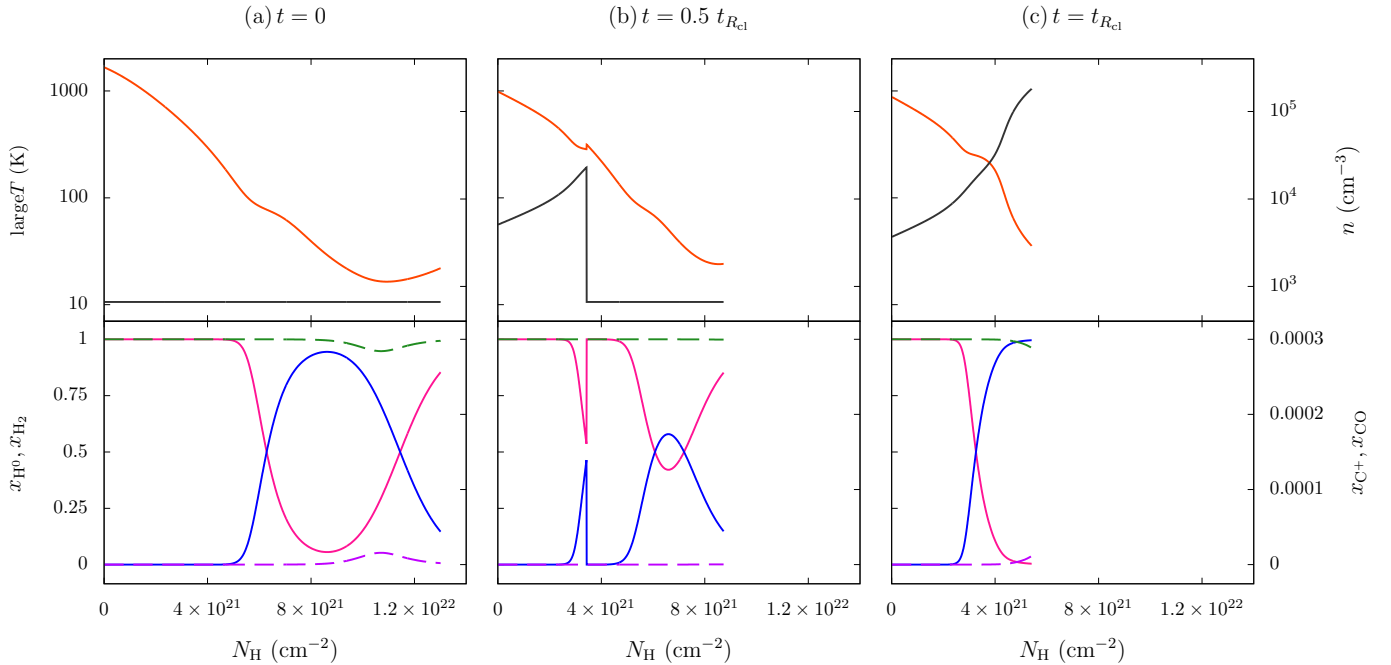


Figure 2. Same as Fig. 1, except for the higher cloud mass of $M_{\text{cl}} = 10^5 M_{\odot}$ and surface density $\Sigma_{\text{cl}} = 300 M_{\odot} \text{pc}^{-2}$.

$S_{\text{EUV}} \simeq 4.2 \times 10^{49} \text{ sec}^{-1}$ and $S_{\text{FUV}} \simeq 8.0 \times 10^{49} \text{ sec}^{-1}$ respectively. Fig. 1 shows the time evolution of the one-dimensional thermal and chemical structure at (a) $t = 0$, (b) $t = 0.5 t_{\text{Rcl}}$, and (c) $t = t_{\text{Rcl}}$, where t_{Rcl} is the time when the shell reaches the cloud edge.

Fig. 1 (a) presents the snapshot at $t = 0$, when the initial Strömgren sphere is created. Since at this epoch the shell has not appeared yet, the density is constant everywhere. The temperature rapidly grows toward the central cluster because of the efficient photoelectric heating by the strong stellar FUV radiation. In the outer part with $1.2 \times 10^{22} \text{ cm}^{-2} \lesssim N_{\text{H}} \lesssim 1.8 \times 10^{22} \text{ cm}^{-2}$, however, the temperature profile is flat since we set the minimum gas temperature at 8 K (see Section 2.3.1). In the lower panel, we see that the hydrogen molecules are dissociated by the cluster FUV radiation for $N_{\text{H}} \lesssim 4.0 \times 10^{21} \text{ cm}^{-2}$.

Fig. 1 (b) shows that the swept-up shell has emerged by the epoch of $t = 0.5 t_{\text{Rcl}}$ and $r_{\text{IF}} = 2.2 \text{ pc}$. The discontinuity of physical quantities at $N_{\text{H}} \simeq 5.4 \times 10^{21} \text{ cm}^{-2}$, which corresponds to the preceding shock front, or the shell outer edge represented by r_{sh} . Within the shell, the temperature decreases outward as the FUV flux drops owing to the dust attenuation. The density inversely increases, because the thermal pressure is assumed to be fixed at the value of the H II region. The hydrogen dissociation front is shifted to the lower column density at $N_{\text{H}} \simeq 2.5 \times 10^{21} \text{ cm}^{-2}$ than in panel (a) because of the efficient self-shielding of H₂ molecules within the dense shell. By contrast, there is only little amount of CO molecules within the shell. The temperature just outside the shell is slightly higher than that inside the shell. Since the density differs by approximately 2 orders of magnitude across the shock front, the cooling efficiency also differs.

Fig. 1 (c) shows the final snapshot for the current case, when all of the cloud materials are swept into the shell. Unlike the previous snapshot, the CO dissociation front is taken into the shell at $N_{\text{H}} \simeq 6.0 \times 10^{21} \text{ cm}^{-2}$ because the shell column density has become so large that CO molecules are protected against the cluster FUV radiation with the dust attenuation. As shown below, this is the final snapshot when the minimum SFE is determined, and the swept-up gas on the shell is, so to speak, the remnant of the molecular cloud. It is evident that the chemical composition of such a cloud remnant is not homogeneous. There are some amount of H₂ molecules, but only a small part of those is associated with CO molecules. We return to this point later in Section 3.3.

Next we show the case where CO molecules are almost completely destroyed by FUV radiation. Fig. 2 represents the case with $M_{\text{cl}} = 10^5 M_{\odot}$ and $\Sigma_{\text{cl}} = 300 M_{\odot} \text{ pc}^{-2}$. The central cluster mass is $2.6 \times 10^4 M_{\odot}$ and corresponding stellar EUV and FUV photon number luminosity is $S_{\text{EUV}} \simeq 1.2 \times 10^{51} \text{ s}^{-1}$ and $S_{\text{FUV}} \simeq 2.5 \times 10^{51} \text{ s}^{-1}$, respectively. The clear difference from the case with $M_{\text{cl}} = 10^4 M_{\odot}$ is that CO molecules do not survive throughout the time evolution. This behavior is mainly explained by the difference of G_0 (see Section 3.3 for detailed discussion).

3.2 Star formation efficiency of molecular clouds

3.2.1 Limiting star formation efficiency by FUV radiation

In this section we investigate the SFE of the molecular clouds set by the EUV and FUV feedback effects. Consider an expanding H II region and surrounding PDR around a newly-born cluster in a given molecular cloud. If the cluster is not sufficiently massive (or luminous), only a small part of the cloud near the cluster would be affected by the feedback; further star formation would occur in the remnant part until enough stars have formed to halt further star formation and destroy the whole cloud. Hence there should be the minimum value of the SFE ϵ_{min} above which the cloud is destroyed by radiative feedback. We calculate ϵ_{min} as functions of M_{cl} and Σ_{cl} in the iterative manner as outlined in Section 2.1.

Each panel in Fig. 3 shows the minimum SFE obtained as a function of the cloud surface density Σ_{cl} for the same mass M_{cl} . The cloud masses of $M_{\text{cl}} = 10^4, 10^5$ and $10^6 M_{\odot}$ are assumed for panels (a), (b) and (c), respectively.

The gray line in each panel represents the case where only the EUV feedback is considered (Criterion 1, $\epsilon_{\text{min},1}$). We see that $\epsilon_{\text{min},1}$ is an increasing function of Σ_{cl} , as shown in Kim et al. (2016). Such a behavior is well understood by considering the Σ_{cl} -dependences of the cloud radius R_{cl} and initial Strömgren radius $r_{\text{St},0}$: $R_{\text{cl}} \propto \Sigma_{\text{cl}}^{-1/2}$ and $r_{\text{St},0} \propto \Sigma_{\text{cl}}^{-1}$ for a given M_{cl} . It means that, with increasing Σ_{cl} , the typical size of the H II region $r_{\text{St},0}$ relative to the cloud size R_{cl} decreases. The more massive or luminous cluster is necessary for the H II region to cover the whole cloud for such a case. Thus the resulting ϵ_{min} is higher for higher surface density. Kim et al. (2016) provide the analytic formula describing this dependence as

$$\frac{\epsilon_{\text{min}}}{(1 - \epsilon_{\text{min}}^2)^2} = \left(\frac{\pi^{5/4} G}{\eta_{\text{th}} \mathcal{T}} \right)^2 M_{\text{cl}}^{1/2} \Sigma_{\text{cl}}^{5/2}, \quad (21)$$

where $\eta_{\text{th}} = 9/4$ and $\mathcal{T} = 8\pi k_{\text{B}} T_{\text{H II}} [3f_{\text{ion}} \Xi_{\text{EUV}} / 4\pi \alpha_{\text{B}}]^{1/2}$. Note that the gray line in each panel representing the EUV feedback is not identical because of the dependence of $\epsilon_{\text{min}} \propto M_{\text{cl}}^{1/2}$ in equation (21).

Let us next examine the effect of the FUV radiation on limiting the minimum SFE. The red line in each panel of Fig. 3 represents the cases with FUV feedback (i.e., Criterion 2, $\epsilon_{\text{min},2}$). Comparing the red line to the gray line, we can evaluate the effect of the FUV feedback on top of the EUV feedback. The minimum SFE is defined as $\epsilon_{\text{min}} = \min(\epsilon_{\text{min},1}, \epsilon_{\text{min},2})$.

Fig. 3 (a) shows that introduction of the FUV feedback does not change the SFEs in the cases with cloud mass $M_{\text{cl}} = 10^4 M_{\odot}$; $\epsilon_{\text{min}} = \epsilon_{\text{min},1}$. For more massive clouds with $M_{\text{cl}} = 10^6 M_{\odot}$ (panel c), by contrast, the FUV feedback is quite important; $\epsilon_{\text{min}} = \epsilon_{\text{min},2}$. For a given Σ_{cl} , the minimum SFE is reduced by the inclusion of the FUV feedback by one order of magnitude, at maximum. In particular, the difference is larger at smaller surface density, Σ_{cl} . In the case with intermediate mass of $M_{\text{cl}} = 10^5 M_{\odot}$ (panel b), the resulting ϵ_{min} is only slightly (by about 10 %) reduced by the FUV feedback effect at the lower and higher ends of Σ_{cl} , i.e., $\Sigma_{\text{cl}} \lesssim 100 M_{\odot} \text{ pc}^{-2}$ and $\Sigma_{\text{cl}} \gtrsim 400 M_{\odot} \text{ pc}^{-2}$.

To summarize, the FUV feedback is sufficiently effective in massive and low surface density clouds. We further

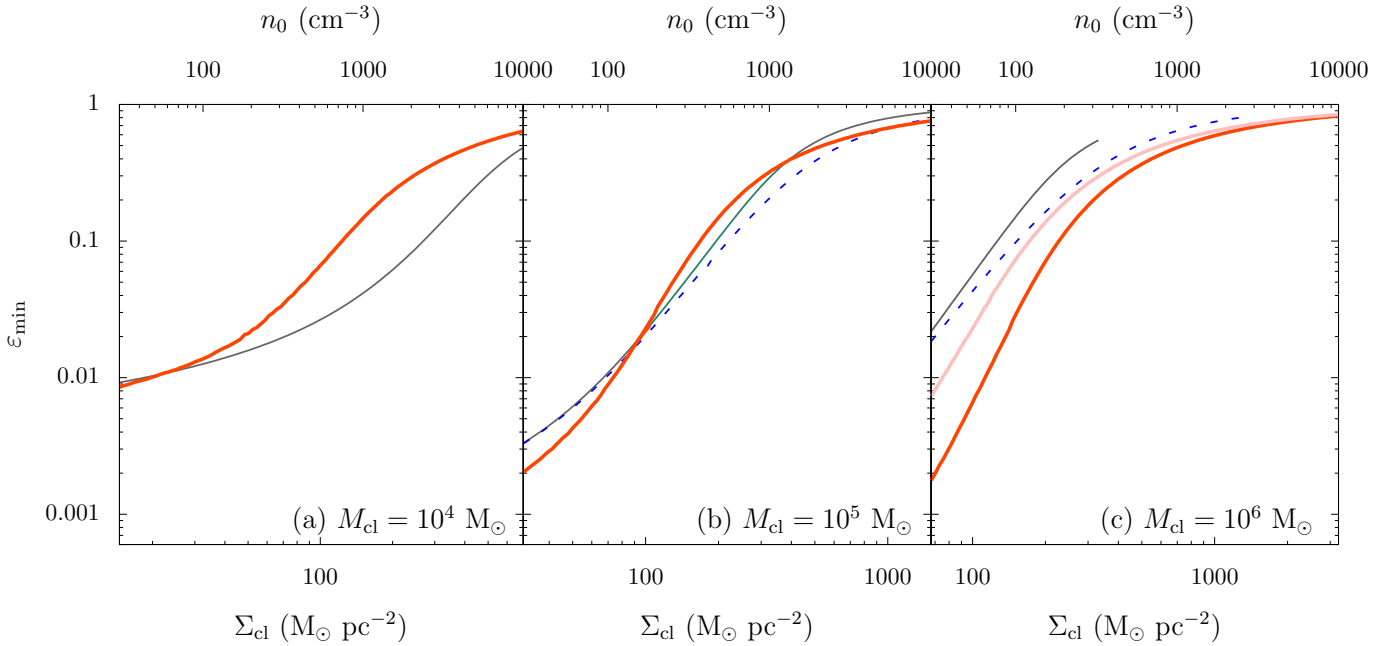


Figure 3. The minimum star formation efficiency (SFE) ε_{\min} calculated as functions of the cloud surface density Σ_{cl} . The different cloud masses of $M_{\text{cl}} = 10^4 M_{\odot}$, $M_{\text{cl}} = 10^5 M_{\odot}$ and $M_{\text{cl}} = 10^6 M_{\odot}$ are assumed for panels (a), (b) and (c). In each panel, the thick red line represents the case where the SFE is limited by both the EUV and FUV feedback (Criterion 2). The gray line represents the reference case only with the EUV feedback (Criterion 1), as considered in Kim et al. (2016). The blue dashed line in panel (b) and (c) represents the cases where effects of the radiation pressure is included for the dynamics of the H II region expansion, and the thin red line in panel (c) represents the cases where the threshold temperature is set to be 300 K (instead of 100 K) in Criterion 2. Note that the different scaling for the horizontal axis are used among the panels.

analyze our calculations to interpret the results in next Section 3.2.2.

3.2.2 Interpreting Results

As shown in Section 3.2.1, the impacts of the FUV feedback on limiting the minimum SFE depends on the cloud parameters such as the cloud mass M_{cl} and surface density Σ_{cl} . Here we further look into our results to consider what causes such variations.

First we investigate the case of clouds with $M_{\text{cl}} = 10^5 M_{\odot}$. Since the heating in PDRs is assumed to limit the SFEs, we consider the temperature just outside of the shell, T_{out} . The thick black line in Fig. 4(a) shows T_{out} as a function of Σ_{cl} at the cloud edge $r = R_{\text{cl}}$ at $t = t_{R_{\text{cl}}}$, i.e., when the SFE is determined by the EUV feedback only (Criterion 1). We see that T_{out} has the local minimum at $\Sigma_{\text{cl}} \approx 200 M_{\odot} \text{pc}^{-2}$. Since the PDR is primarily heated up via the photoelectric emission from grains, the local FUV flux G_{out} is a key quantity to determine T_{out} . According to equations (1) and (18), G_{out} is proportional to $S_{\text{FUV}} \Sigma_{\text{cl}} / M_{\text{cl}} \propto \varepsilon_{\min} \Sigma_{\text{cl}}$ (neglecting dust attenuation). It follows that G_{out} monotonically increases with increasing Σ_{cl} , because the minimum SFE or S_{FUV} increases with Σ_{cl} (Fig. 3a). With the above facts, one may ask why T_{out} decreases with Σ_{cl} for $\Sigma_{\text{cl}} \lesssim 200 M_{\odot} \text{pc}^{-2}$, where G_{out} increases with Σ_{cl} . This is explained by the nature of the [C II] line cooling, which dominates over other processes. The [C II] cooling rapidly becomes efficient with the increasing density n (or Σ_{cl}) for $n \ll n_{\text{cr}} \approx 2000 \text{ cm}^{-3}$. Such a trend is illustrated as gray lines in Fig. 4, which show

the equilibrium gas temperature as a function of density at for different values of G_{out} clearly show such a trend. Since the slope of the contour lines are so steep that T_{out} drops while G_{out} increases with Σ_{cl} .

Let us compare T_{out} with the threshold temperature for the FUV feedback, 100 K. We see that T_{out} exceeds 100 K in both the lower and higher sides of Σ_{cl} . It suggests that the destruction by the FUV feedback is more effective than dynamical disruption. Since the temperature gets lower with the lower G_{out} at a given Σ_{cl} , only the smaller S_{FUV} (or smaller ε) is enough to realize $T_{\text{out}} = 100 \text{ K}$. The above explains why ε is reduced by the FUV feedback in the higher and lower sides of Σ_{cl} in Fig. 3.

Fig. 4(b) shows the same plots as Fig. 4(a) but for the cases with more massive clouds with $M_{\text{cl}} = 10^6 M_{\odot}$, where the FUV feedback effects are more remarkable than other cases. In this case, T_{out} is much higher than the threshold temperature 100 K for any range of Σ_{cl} . This is due to the dependence of $G_{\text{out}} \propto S_{\text{FUV}} \Sigma_{\text{cl}} / M_{\text{cl}}$ again. With a fixed value of Σ_{cl} , G_{out} is larger with the higher M_{cl} because $G_{\text{out}} \propto \varepsilon S_{\text{FUV}} / M_{\text{cl}} = \varepsilon \Xi_{\text{FUV}}$ and ε is enhanced following equation (21). The SFEs required to disrupt the natal cloud is much smaller than the case only with the EUV feedback. Fig. 4(b) also suggests that even with somewhat large threshold temperature $\lesssim 700 \text{ K}$ the FUV feedback should still reduce the minimum SFE ε_{\min} .

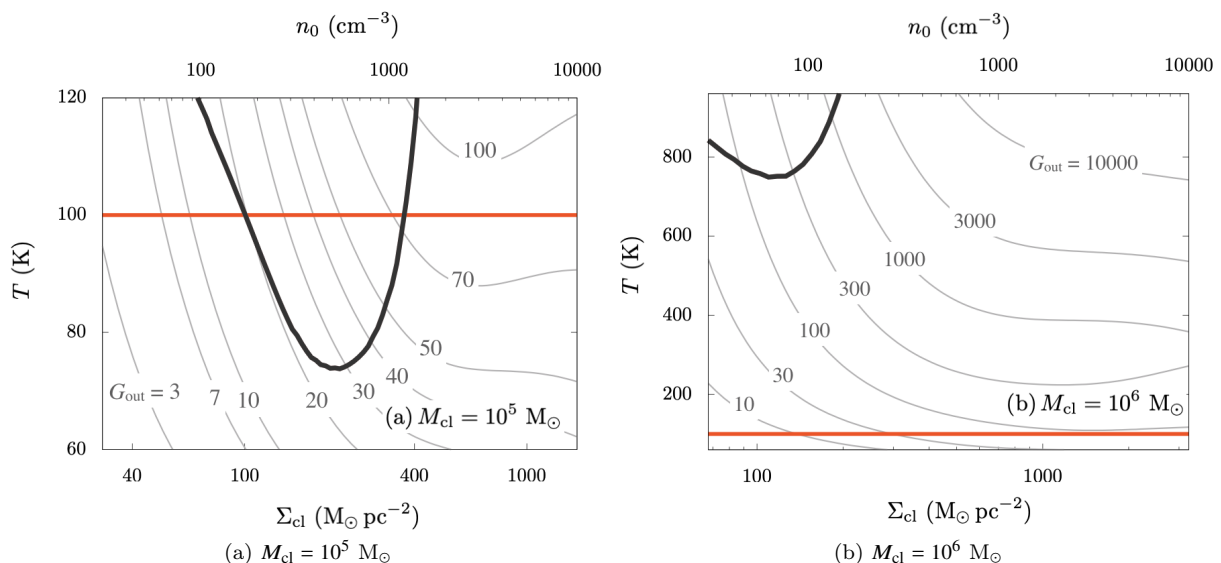


Figure 4. Effects of the FUV heating in limiting the minimum SFE with $M_{\text{cl}} = 10^5 M_{\odot}$ (panel a) and $M_{\text{cl}} = 10^6 M_{\odot}$ (b). In each panel, the thick black line represents the gas temperature at the cloud outer edge when the minimum SFE is determined only by the EUV feedback (Criterion 1, the gray lines in Fig. 3). In such a case, an expanding H II region and surrounding shell just fill the whole cloud, and the “cloud edge” corresponds to the un-shocked gas just outside the shell. The red line represents the critical temperature 100 K, above which the star formation is assumed to be suppressed by the FUV feedback (Criterion 2). At Σ_{cl} for which the red curve exceeds the red line, the gas is heated up above 100 K before the shell reaches the cloud edge, meaning that the SFE should be primarily limited by the FUV feedback if included. The gray contours denote the equilibrium temperature for different values of FUV flux G_{out} as functions of the density. We note that, in panel (b), the vertical axis covers the much larger range of the temperature than in panel (a).

3.3 Chemical compositions of molecular cloud remnants

Our calculations suggest that the EUV and FUV radiative feedback from forming clusters jointly contribute to reduce the SFE of molecular clouds. In this section, we cast light on the gas that has not been used for the star formation, i.e., the “remnants” of the clouds. The cloud remnants still retain a large part of the cloud materials because the obtained SFEs are much smaller than the unity for many cases. We here focus on the chemical compositions of the cloud remnants, which are also followed in our calculations.

We calculate the masses of H I, CO-dark and CO-bright H_2 gases as follows:

$$M_{\text{H I}} = \sum_{k=0}^N 4\pi r_k^2 \mu_{\text{H}} \Delta N_{\text{H}} x_{\text{H}^0}, \quad (22)$$

$$M_{\text{H}_2 \text{ w/o CO}} = \sum_{k=0}^N 4\pi r_k^2 \mu_{\text{H}} \Delta N_{\text{H}} x_{\text{H}_2} x_{\text{C}^+} / x_{\text{C}}, \quad (23)$$

$$M_{\text{H}_2 \text{ w/ CO}} = \sum_{k=0}^N 4\pi r_k^2 \mu_{\text{H}} \Delta N_{\text{H}} x_{\text{H}_2} x_{\text{CO}} / x_{\text{C}}. \quad (24)$$

First we consider the cases with the fixed cloud mass $M_{\text{cl}} = 10^5 M_{\odot}$. Fig. 5 (a) presents the mass fraction of the gas with the different chemical properties as functions of Σ_{cl} . The neutral and molecular hydrogens are the dominant components of the cloud remnants, and they occupy 70 % and 30 % of the total mass respectively. In particular, we distinguish H_2 molecules associated with CO molecules and those without CO. The H_2 gas without CO molecules is the so-called “CO-dark” molecular gas. Let us see the cases where the minimum SFE is limited by the EUV and FUV feed-

back (Criterion 2, solid lines). Fig. 5 (a) shows that most of the H_2 molecules contained in the remnants are actually CO-dark. Such a trend only has a weak dependence on Σ_{cl} ; the mass of the CO-dark H_2 gas is generally much less than 10 % of that of the H_2 gas associated with CO molecules. This is caused by the different shielding processes of H_2 and CO molecules. As shown in Fig. 5(c), the column density of the shell is roughly $N_{\text{H}}^{\text{shell}} \approx 2 - 7 \times 10^{21} \text{ cm}^{-2}$, corresponding to $A_{\text{V}} \approx 1 - 3.5$. The dust attenuation of the FUV radiation is not very efficient for such cases. In fact, Fig. 5(b) shows that the FUV flux at the shock front G_{out} is several to several tens, which is high enough to photodissociate CO molecules. On the other hand, H_2 molecules are protected against the FUV radiation by the self-shielding effect even with the small column densities. Since the self-shielding is not available for CO molecules, which only have the small abundance, CO molecules are selectively destroyed.

We also investigate how the above properties are altered when we only consider the EUV feedback (see the thin symbols connected with dashed lines in Fig. 5). For such cases, only the quantities for $\Sigma_{\text{cl}} \gtrsim 300 M_{\odot} \text{ pc}^{-2}$ are modified. Fig. 5(a) shows that the amount of H_2 with CO molecules are further reduced for such large Σ_{cl} . Fig. 5(c) explains it is caused by the decline of the shell column density $N_{\text{H}}^{\text{shell}}$. We see that $N_{\text{H}}^{\text{shell}}$ rather turns to decrease with Σ_{cl} for $\Sigma_{\text{cl}} \gtrsim 300 M_{\odot} \text{ pc}^{-2}$. Fig. 5(b) shows that G_{out} accordingly rises with Σ_{cl} , resulting in the efficient dissociation of CO molecules.

The above dependence on the feedback criteria is actually well understood with the following analytic arguments.

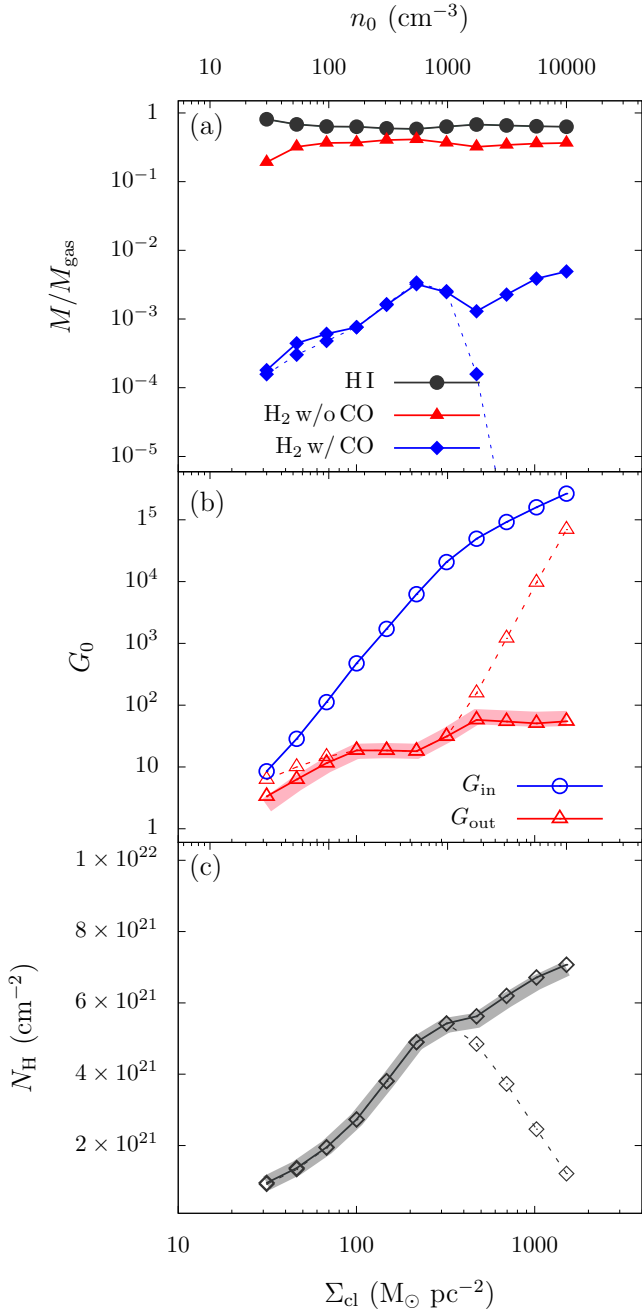


Figure 5. Chemical compositions of the gas that has not been converted into stars (molecular cloud “remnants”, panel a) and relevant quantities (panel b and c). The same cloud mass of $M_{\text{cl}} = 10^5 M_{\odot}$ is assumed for the different cloud surface densities Σ_{cl} as in Fig. 3. *Panel (a)*: the mass fractions relative to the total remnant mass for the different chemical properties: H I (black filled circles), H_2 without CO (red filled triangles), and H_2 with CO (blue filled squares). *Panel (b)*: FUV fluxes throughout the shell. The blue open circles represent the incident FUV flux at the ionization front, and the red open triangles represent that at the preceding shock front. *Panel (c)*: The hydrogen column density of the shell. In each panel, the symbols connected by the solid lines represent the cases where the minimum SFEs are limited by the EUV and FUV feedback. We also show the cases only with the EUV feedback with the thin symbols connected by the dashed lines. In panels (b) and (c), the thick solid lines represent the analytic evaluations of G_{out} and $N_{\text{H}}^{\text{shell}}$ by equations (30) and (29).

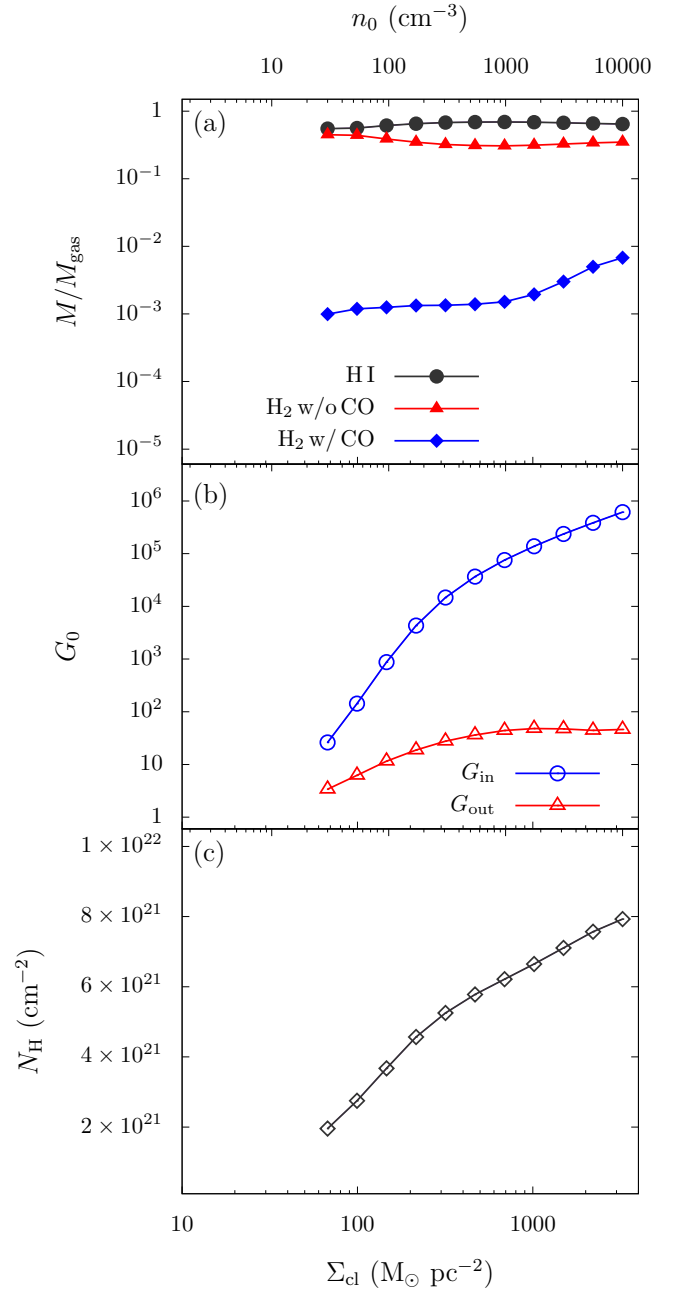


Figure 6. Same as Fig. 5 but for the higher cloud mass of $M_{\text{cl}} = 10^6 M_{\odot}$. In the top panel, the H_2 -with-CO fraction for the cases only with the EUV feedback is not presented because it is far below 10^{-5} .

Since the ionized gas density (at $t = t_{R_{\text{cl}}}$) is given by

$$n_{\text{HII}} = \sqrt{\frac{3S_{\text{EUV}}f_{\text{ion}}}{4\pi R_{\text{cl}}^3 a_{\text{B}}}}, \quad (25)$$

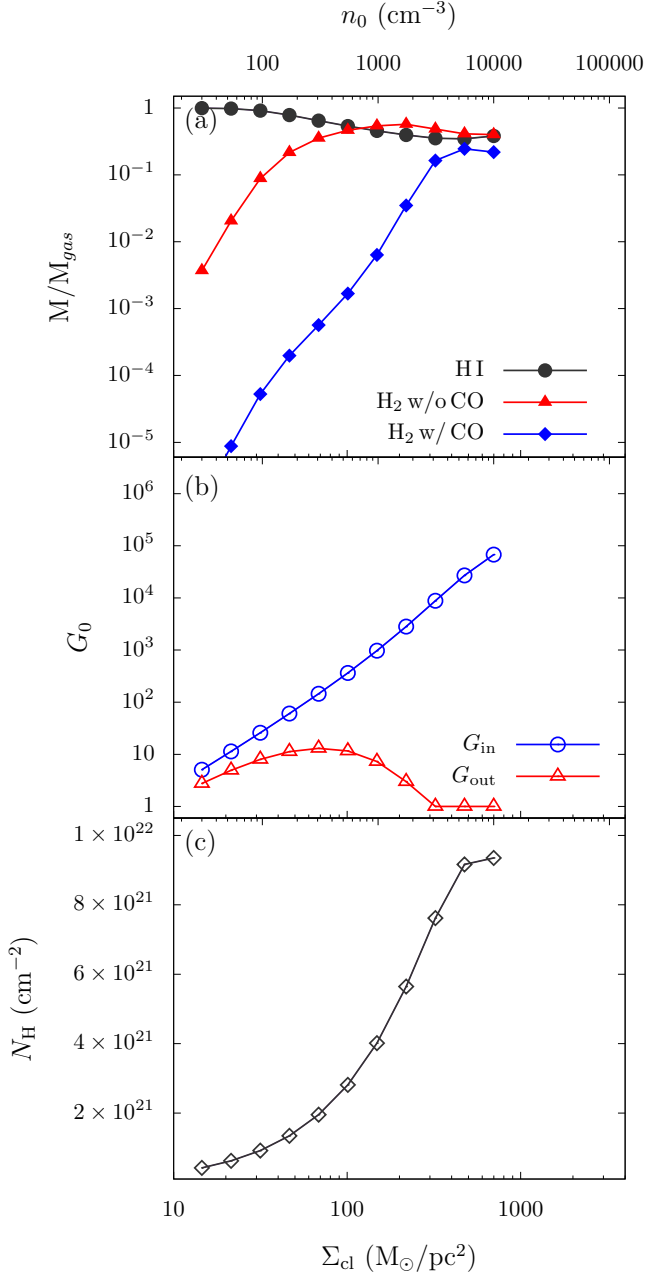


Figure 7. Same as Fig. 5 but for the lower cloud mass of $M_{\text{cl}} = 10^4 M_{\odot}$. We here do not present the cases only with the EUV feedback unlike Figs. 5 and 6, because the resulting minimum SFE is exactly the same (see Section 3.2.1).

the mass of the ionized gas can be written as

$$\begin{aligned}
 M_{\text{H II}} &= \frac{4}{3} \pi R_{\text{cl}}^3 \mu_{\text{H}} n_{\text{H II}} \\
 &= \mu_{\text{H}} \left(\frac{4 f_{\text{ion}} \Xi_{\text{EUV}}}{3 \alpha_{\text{B}} \pi^{1/2}} \right)^{1/2} \varepsilon^{1/2} M_{\text{cl}}^{5/4} \Sigma_{\text{cl}}^{-3/4} \\
 &= 1.2 \times 10^4 M_{\odot} \left(\frac{\varepsilon}{0.01} \right)^{1/2} \left(\frac{M_{\text{cl}}}{10^5 M_{\odot}} \right)^{5/4} \left(\frac{\Sigma_{\text{cl}}}{10^2 M_{\odot}/\text{pc}^2} \right)^{-3/4}.
 \end{aligned} \tag{26}$$

Since the ratio $M_{\text{H II}}/M_{\text{cl}}$ depends only weakly on M_{cl} and

Σ_{cl} , we take $M_{\text{H II}} \sim 0.1 M_{\text{cl}}$. Then, the shell column density $N_{\text{H}}^{\text{shell}}$ and FUV flux at the shock front G_{out} obey the following relations

$$\begin{aligned}
 M_{\text{shell}} &= M_{\text{cl}}(1 - \varepsilon) - M_{\text{H II}} \approx 4\pi R_{\text{cl}}^2 \mu_{\text{H}} N_{\text{H}}^{\text{shell}} \\
 \rightarrow N_{\text{H}}^{\text{shell}} &= \frac{\Sigma_{\text{cl}}}{4\mu_{\text{H}}} \left(1 - \varepsilon - \frac{M_{\text{H II}}}{M_{\text{cl}}} \right) \\
 &\sim \frac{\Sigma_{\text{cl}}}{4\mu_{\text{H}}} (0.9 - \varepsilon),
 \end{aligned} \tag{28}$$

$$\sim \frac{\Sigma_{\text{cl}}}{4\mu_{\text{H}}} (0.9 - \varepsilon), \tag{29}$$

$$\begin{aligned}
 G_{\text{out}} &= \frac{1}{F_{\text{H}}} \frac{S_{\text{FUV}}}{4\pi R_{\text{cl}}^2} \exp(-\sigma_{\text{d}} N_{\text{H}}^{\text{shell}}) \\
 &\sim \frac{\varepsilon \Xi_{\text{FUV}}}{4F_{\text{H}}} \Sigma_{\text{cl}} \exp \left[-\frac{\sigma_{\text{d}}}{4\mu_{\text{H}}} \Sigma_{\text{cl}} (0.9 - \varepsilon) \right].
 \end{aligned} \tag{30}$$

The factor of $(0.9 - \varepsilon)$ in the above equations is actually important to understand the results. Fig. 3(a) shows that, for $\Sigma_{\text{cl}} \gtrsim 300 M_{\odot}/\text{pc}^2$, ε_{min} only slightly changes with whether the FUV feedback is included or not. Since ε_{min} is close to 0.9, however, the resulting change of $(0.9 - \varepsilon)$ is large. Only with the EUV feedback $(0.9 - \varepsilon)$ significantly declines, meaning that there is only little amount of the remnant gas that shields the FUV radiation. If follows that the shell column density declines for $\Sigma_{\text{cl}} \gtrsim 300 M_{\odot}/\text{pc}^2$ for such cases.

We have performed the same analyses as above also for the cases with the different cloud masses $M_{\text{cl}} = 10^6 M_{\odot}$ and $10^4 M_{\odot}$. Fig. 6 presents the former cases with the large cloud mass $10^6 M_{\odot}$. Again, most of the hydrogen molecules contained in the cloud remnants are not associated with CO molecules (Fig. 6a). If we only consider the EUV feedback, we can hardly find CO molecules remained. The shell column density $N_{\text{H}}^{\text{shell}}$ is only less than $2 \times 10^{21} \text{ cm}^{-2}$ (panel b), and the dust attenuation hardly contributes to reduce the FUV flux throughout the remnant gas (panel c).

Similarly, Fig. 7 presents the cases with the low-mass clouds with $M_{\text{cl}} = 10^4 M_{\odot}$. Recall that the minimum SFE does not depend on whether the FUV feedback is considered or not for this case. We see the higher fractions of H_2 gas associated with CO molecules than the previous cases, in particular, for $\Sigma_{\text{cl}} \gtrsim 300 M_{\odot}/\text{pc}^2$ (panel a). The above analytic formulae are again useful to interpret such a variation. Since $\varepsilon_{\text{min}} \ll 1$ for the current cases (see equation 21), the factor of $(0.9 - \varepsilon)$ is just regarded as a constant. The combination of equations (29) and (30) leads to $N_{\text{H,shell}} \propto \Sigma_{\text{cl}}$ and $G_{\text{out}} \propto \varepsilon \Xi_{\text{FUV}} \exp(-\Sigma_{\text{cl}})$, indicating that the FUV flux rapidly drops with increasing Σ_{cl} because the shell column density increases. Indeed, the column density $N_{\text{H,shell}}$ monotonically increases with increasing Σ_{cl} (panel c). The FUV flux G_{out} decreases in concert, as predicted by equation (30). For $\Sigma_{\text{cl}} \gtrsim 300 M_{\odot}/\text{pc}^2$, G_{out} is just limited by the background value $G_{\text{out}} = 1$ (panel b). The above facts suggest that the FUV radiation from the cluster is substantially attenuated by the dust grains. As a result, a certain amount of CO molecules survives, being protected against the dissociating photons.

4 DISCUSSION

4.1 Validity of thermal and chemical equilibrium

We have assumed the thermal and chemical equilibrium in our modeling. We here examine the validity of such as-

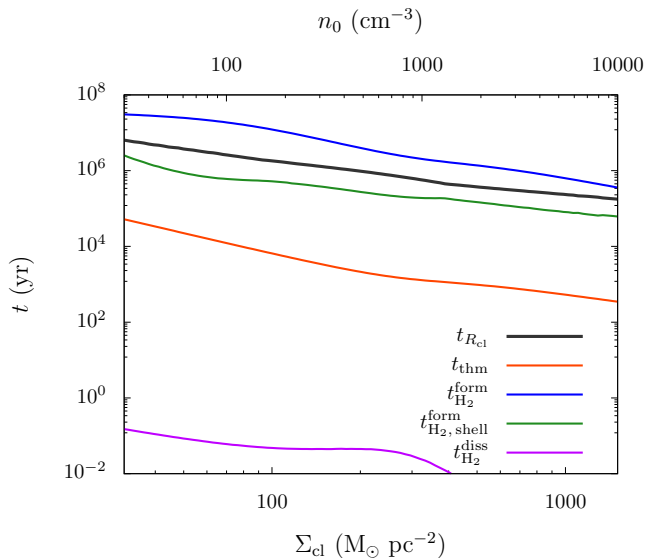


Figure 8. Comparisons of various characteristic timescales in our calculations with $M_{\text{cl}} = 10^5 M_{\odot}$ and different cloud surface density Σ_{cl} . The snapshots when the minimum SFE is determined with our Criterion 2 are used. Presented are the shell expansion timescale $t_{R_{\text{cl}}}$ (black line), cooling time at the cloud edge (at $r = R_{\text{cl}}$, red line), H_2 formation time at the cloud edge (blue line) and on the shell (green line) and H_2 dissociation time at cloud edge (purple line). The average shell density is calculated by equation (34.)

assumptions. In order to do that, we evaluate the timescales over which the thermal and chemical equilibrium states are achieved, t_{thm} and t_{chem} . In particular, we consider the H_2 equilibrium timescale t_{H_2} as t_{chem} because its formation reaction on the grain surface is slowest among the included reactions. We calculate t_{thm} and t_{H_2} by the same method as in Koyama & Inutsuka (2000).

$$t_{\text{thm}} = e/\Gamma, \quad (31)$$

$$t_{\text{H}_2}^{\text{form}} = x_{\text{H}_2}/R_{\text{H}_2}^{\text{form}}, \quad (32)$$

$$t_{\text{H}_2}^{\text{diss}} = x_{\text{H}_2}/R_{\text{H}_2}^{\text{diss}}. \quad (33)$$

where $R_{\text{H}_2}^{\text{form}}$ and $R_{\text{H}_2}^{\text{diss}}$ are the formation and dissociation rates of H_2 molecules, respectively (see equation 13). We use the snapshots at the epochs when the expanding shell reaches the cloud edge at $r = R_{\text{cl}}$, i.e., $t = t_{R_{\text{cl}}}$, where the expansion timescale $t_{R_{\text{cl}}}$ corresponds to the dynamical timescale. The input parameters for calculation are $n = n_0$, $G_0 = G_{\text{out}}$, and $N_{\text{H}} = N_{\text{H}}^{\text{shell}}$ [Fig. 8 (b) and (c)]. Inside shell, in contrast, average density is

$$\bar{n} = N_{\text{H}}^{\text{shell}}/dR, \quad (34)$$

where dR is geometrical thickness of the shell, while G_0 and N_{H} are the same as those in the outside the shell (this treatment is not so accurate, but is a reasonable approximation).

In Fig. 8 we present the above timescales as functions of Σ_{cl} for the cases with $M_{\text{cl}} = 10^5 M_{\odot}$. We see that all the timescales gradually decrease with increasing Σ_{cl} . The dynamical timescale $t_{R_{\text{cl}}} \propto R_{\text{cl}}/c_{\text{s,H II}}$ decreases, because the higher Σ_{cl} is the smaller becomes the cloud size for a fixed cloud mass (equation 1). The chemical and thermal

timescales also drop because collisions, which drive the dominant cooling and chemical processes, occur more efficiently with the higher density. The figure shows that the thermal equilibrium timescale is always much shorter than the dynamical time, thus supporting our assumption of the thermal equilibrium.

The chemical equilibrium should hold within the dense shell, which carries most of the remnant gas, since the H_2 formation timescale is comparable to or shorter than the dynamical time $t_{R_{\text{cl}}}$ (see the green line). By contrast, the H_2 formation timescale is somewhat longer than $t_{R_{\text{cl}}}$ at the cloud edge (see the blue line). It means that the chemical equilibrium of H_2 molecules may not be achieved in the un-shocked ambient medium outside of the shell by the end of the calculations. However, the clouds we consider are initially fully molecular so that the chemical equilibrium should always be a good assumption even for H_2 , since the dissociation timescale is much shorter than the formation timescale (see the purple line). Therefore our conclusion on the chemical composition presented in Section 3.3 will not change much even if we include the non-equilibrium effects.

4.2 Effects ignored

As already mentioned in Section 2.3.1, our 1D models of the PDR use assumptions for simplicity, e.g., the optically thin fine-structure line cooling and constant dust temperature throughout a PDR. In order to examine the validity of our treatments, we have also calculated the dynamical evolution of an H II region and surrounding PDR using a 1D radiation-hydrodynamics (RHD) code developed in Hosokawa & Inutsuka (2006) for several representative cases. The RHD code takes the effects ignored in the semi-analytic models into account, such as the trapping effect of the line emission and variable dust temperature. We have confirmed that the simulation results show the similar overall structure of the PDR as provided by the semi-analytic models in spite of the numerous differences. For instance, the evolution of the average density within the shell only differs by a few $\times 10\%$ between the RHD simulations and the semi-analytic models.

Although our RHD simulations and semi-analytic models employ the same method of Nelson & Langer (1999) for the CO formation rate, there are differences in evaluating the CO photodissociation rate. The semi-analytic models only use the FUV intensity G_i , for which the dust attenuation law is given by the cross section $\sigma_{\text{d}} = 10^{-21} \text{ cm}^2 \text{H}^{-1}$, to evaluate the CO dissociation rate. The RHD simulations, on the other hand, consider another FUV component only representing the CO dissociating band, for which the dust cross section is somewhat larger than the averaged value for the full FUV range $6 \text{ eV} \leq h\nu \leq 13.6 \text{ eV}$. Moreover, the RHD simulations also incorporate the effects of self- and H_2 -shielding of CO molecules against dissociating photons (e.g., van Dishoeck & Black 1988). The semi-analytic models thus tend to overestimate the CO photodissociation rate, ignoring these effects. In order to evaluate this effect, we have compared the simulation and model results for the case with $M_{\text{cl}} = 10^5 M_{\odot}$ and surface density $\Sigma_{\text{cl}} = 300 M_{\odot} \text{ pc}^{-2}$ (e.g., see Figs. 2 for the model). As shown in Figure 5, the model predicts that only $\sim 0.1\%$ of the cloud remnant should be H_2 molecular gas associated with CO molecules. The RHD simulation run with the same setting shows that this quantity is $\sim 1\%$ at

the epoch when the expanding shell reaches the cloud edge, $t \simeq 6 \times 10^5$ years since the birth of the H II region. We interpret that such a high value in the simulation run is due to the CO dissociation rate overestimated in the model. If we ignore the effects which are not considered in the model, the simulation returns the lower value ~ 0.03 %. We have also found that the value rapidly rises in the corresponding stage, varying by an order of magnitude in $\sim 10^5$ years. We conclude that, while there is the general trend that most of the molecular gas contained in the cloud remnants should be CO-dark, the exact amount of the CO-bright molecular gas is difficult to be accurately estimated.

4.3 Other stellar feedback processes

In order to isolate potential roles of the FUV feedback during the cloud disruption, we have employed the simple assumption on the H II bubble expansion, i.e., that the thermal pressure excess of the photoionized gas with respect to the ambient medium drives the expansion. As briefly noted in Section 2.2, theoretical studies suggested that radiation pressure exerted on the shell affects the expansion motion (e.g., Krumholz & Matzner 2009; Fall et al. 2010; Murray et al. 2010; Kim et al. 2016). Such studies all show that the expansion is mainly driven by the radiation pressure rather than the gas pressure if $\Sigma_{\text{cl}} \gtrsim 100 \text{ M}_{\odot}\text{pc}^{-2}$, which is also confirmed by recent numerical simulations, although for turbulent clouds the transition occurs at somewhat higher Σ_{cl} (e.g., Kim et al. 2018). Kim et al. (2016) have actually incorporated the effect of the radiation pressure in their model by taking $F_{\text{rad}} = L/c$ as the average radiation force. We also follow the same approach as theirs to modify the temporal evolution of the shell radius given by equation (10). The resulting minimum SFEs for such cases are also presented by the blue dashed line in Fig. 3(b), for which only the EUV feedback is assumed (Criterion 1) with $M_{\text{cl}} = 10^6 \text{ M}_{\odot}$. We find that the radiation pressure effect further reduces ε_{min} , and that its effect is more prominent for the higher Σ_{cl} . Inversely, the FUV feedback are effective for the low surface density $\Sigma_{\text{cl}} \lesssim 100 \text{ M}_{\odot}\text{pc}^{-2}$ (Section 3.2.1), for which the effect of the radiation pressure is limited.

Stellar winds from high-mass stars are also omitted in our models, though they have been referred to as the main driver of the bubble around a massive cluster including many O-type stars (e.g., McKee et al. 1984). The dynamics of the wind-driven bubbles has been modeled assuming the spherical symmetry (e.g., Weaver et al. 1977), and it is well described by an expansion law which differs from equation (10). Recent studies further investigate the interplay between the radiation pressure and stellar winds during the bubble expansion (e.g., Rahner et al. 2017, 2019). Since we have focused on the FUV feedback based on the model of Kim et al. (2016), we have ignored the wind effects following their approach. Regarding the minimum SFEs, we have shown that the FUV feedback is effective for massive GMCs with $M_{\text{cl}} \gtrsim 10^5 \text{ M}_{\odot}$ (Section 3.2). The stellar winds may affect the bubble dynamics for such cases, where the birth of massive clusters with $\gtrsim 10^3 \text{ M}_{\odot}$ is supposed assuming $\varepsilon \sim 0.01$. We have also shown that the FUV radiation produces the CO-dark gas even for the less massive clouds with $M_{\text{cl}} \lesssim 10^5 \text{ M}_{\odot}$ (Section 3.3). The star cluster considered is relatively small with a few O-type stars at most, for which

the wind effect should be limited. In any rate, recent studies point out that the wind effects on the bubble expansion should be overestimated in 1D modeling. Multi-dimensional simulations show that the hot gas generated in the wind-driven bubble actually quickly leaks out through low-density channels rather than being confined (e.g., Rogers & Pittard 2013). There are no clear observational signatures that the bubble expansion is evidently driven by the winds (e.g., Lopez et al. 2014). We note that multi-dimensional effects should also affect the H II bubble dynamics even without the wind effects, which is further discussed in Section 4.4.

In this paper, we have considered the stellar feedback on GMCs before the first supernova explosion occurs. As presented in Fig. 8, the dynamical timescale of an H II bubble expansion is longer for the lower cloud surface density, \simeq several \times Myr for $\Sigma_{\text{cl}} \lesssim 100 \text{ M}_{\odot}\text{pc}^{-2}$. This is still shorter than the lifetime of high-mass stars that cause the supernova explosions ~ 10 Myr, but there may not be a long time lag. It is interesting to speculate what happens if a supernova explosion occurs within a clouds under the stellar FUV feedback. Since the supernova explosion add mechanical feedback on the cloud, it further contributes to reduce the SFE. Moreover, shock waves around the expanding supernova remnant sweep up the gas of the cloud being destroyed, which contains the CO-dark gas under the FUV feedback. Since the shock compression is a possible channel of the molecular cloud formation (e.g. Inoue & Imutsuka 2008, 2009), the CO-dark gas may be brought back into ‘‘CO-bright’’ molecular phase once the FUV radiation is somehow attenuated.

4.4 Inhomogeneous cloud density structure

In our one-dimensional semi-analytic modeling, we have assumed the homogeneous density distribution within a molecular cloud. It is actually possible to relax such an assumption by improving our current model. Kim et al. (2016) have also considered cases with the power-law density distributions $\rho \propto r^{-w}$ with $w < 1.5$. In general, the photoionized gas expands more rapidly with the less efficient ‘‘trapping’’ for the cloud with the steeper density gradient (e.g., Franco et al. 1990). An extreme case is known as the ‘‘champagne flow’’ or ‘‘blister-type’’ H II regions (e.g., Tenorio-Tagle 1979), for which the gas motion is not adequately described as the pressure-driven expanding shell, but rather as the photoevaporation where the ionized gas freely escapes from the cloud. Fully investigating the FUV feedback with such a variety of dynamical evolution is out of scope of the current work, but further studies are warranted (e.g., Hosokawa 2007; Geen et al. 2019).

In order to consider the more realistic clumpy cloud structure, one has to resort to 3D radiation-hydrodynamics numerical simulations. A number of authors in fact have conducted such simulations mostly focusing on the stellar EUV feedback (Section 1). Simulations by Kim et al. (2018) have followed the EUV feedback against clumpy and turbulent GMCs to drive SFEs as functions of the cloud masses and surface densities. They have confirmed the qualitative agreements with Kim et al. (2016)’s model predictions, but also found that the model underestimates minimum SFEs compared to the simulation results. The simulations show that the ionized gas escapes from a cloud through low-density parts and the actual feedback is dominated by photoevapo-

ration of surviving clumps. The FUV feedback in the clumpy medium has yet to be fully studied by similar numerical approaches (e.g., [Arthur et al. 2011](#)). Although we just have assumed that the star formation is locally quenched in a warm PDR (Section 2.4), it should be also verified with such simulations. Note that the star formation might be rather induced in a clumpy PDR because pre-existing clumps exposed to the FUV radiation would be compressed via the radiation-driven implosion (e.g., [Gorti & Hollenbach 2002](#); [Nakatani & Yoshida 2018](#)).

5 CONCLUSION

We have developed a semi-analytic model to investigate the FUV feedback on molecular clouds, particularly effects on the thermal and chemical states of the irradiated gas. On the basis of the previous model by [Kim et al. \(2016\)](#), we have solved the thermal and chemical structure of the PDR as well as the dynamical expansion of an HII region assuming spherical symmetry. We have first evaluated the impacts of the FUV feedback on the resulting minimum SFEs supposing that the star formation is suppressed in the warm PDR where the temperature is more than a threshold value, i.e., ~ 100 K. We have also calculated the chemical composition of the gas that is not converted to stars, i.e., the cloud remnants, under the FUV radiation from the newborn star cluster.

Following [Kim et al. \(2016\)](#), we have calculated the minimum SFEs as functions of the cloud surface density Σ_{cl} for different cloud masses of $M_{\text{cl}} = 10^4, 10^5, 10^6 M_{\odot}$. We argue that the FUV feedback is more effective than the pure EUV feedback caused only by the expansion of the HII regions, particularly for massive clouds with $M_{\text{cl}} > 10^5 M_{\odot}$ and with the low surface density, $\Sigma_{\text{cl}} < 100 M_{\odot} \text{ pc}^{-2}$. The minimum SFEs are reduced by the FUV feedback by no less than an order of magnitude when the star formation is assumed to be suppressed above the threshold temperature, 100 K. A key quantity to interpret such dependencies is the FUV flux at the cloud edge $r = R_{\text{cl}}$ when the cloud is assumed to be disrupted by the EUV feedback, G_{out} . If G_{out} is large enough, it means that the cloud is sufficiently heated up by the FUV radiation before the EUV feedback operates, suggesting that the minimum SFE is predominantly determined by the FUV feedback. Our analyses show the scaling relation $G_{\text{out}} \propto M_{\text{cl}}^{1/2} \Sigma_{\text{cl}}^{7/2}$, which explains why the FUV feedback is more effective with the higher M_{cl} . The same scaling suggests that G_{out} is rather smaller with the lower Σ_{cl} for a given cloud mass M_{cl} , which apparently contradicts with the trend that the FUV feedback is more effective for the lower Σ_{cl} . The discrepancy is explained by the fact that the [C II] line cooling, the dominant process, becomes inefficient sharply with decreasing Σ_{cl} (or the volume density for a fixed M_{cl}). Owing to this, the cloud gas tends to be easily heated up even by the weak FUV radiation field. Therefore, the minimum SFE is limited primarily by the FUV feedback with the lower Σ_{cl} .

Moreover, our analyses on the chemical compositions of the cloud remnants suggest that a large part of them are actually “CO-dark”, except for the cases with $M_{\text{cl}} = 10^4 M_{\odot}$ and $\Sigma_{\text{cl}} > 300 M_{\odot} \text{ pc}^{-2}$. This is because the column densities of the cloud remnants are $2 - 7 \times 10^{21} \text{ cm}^{-2}$ with the

wide range of parameters M_{cl} and Σ_{cl} . With such small column densities corresponding to $A_{\text{V}} \approx$ a few, CO molecules within the cloud remnants are not protected against the incident FUV radiation by the dust attenuation. Only hydrogen molecules survive with the efficient self-shielding effect by contrast. We have also confirmed that such a feature should be the same even for cases where the minimum SFE is primarily limited by the EUV feedback, i.e., where the stellar FUV radiation only plays a minor role in destroying the natal clouds. The dispersed molecular clouds are potential factories of the CO-dark gas, which returns into the cycle of the interstellar medium.

ACKNOWLEDGEMENTS

We thank Shu-ichiro Inutsuka for fruitful discussion and comment. This work is financially supported by the Grants-in-Aid for Basic Research by the Ministry of Education, Science and Culture of Japan (16H05996, 19H01934: T.H.).

REFERENCES

- Arthur S. J., Henney W. J., Mellema G., de Colle F., Vázquez-Semadeni E., 2011, *MNRAS*, **414**, 1747
- Bakes E. L. O., Tielens A. G. G. M., 1994, *ApJ*, **427**, 822
- Bisbas T. G., et al., 2015, *MNRAS*, **453**, 1324
- Butler M. J., Tan J. C., Teyssier R., Rosdahl J., Van Loo S., Nickerson S., 2017, *ApJ*, **841**, 82
- Chabrier G., 2003, *PASP*, **115**, 763
- Clark P. C., Glover S. C. O., Klessen R. S., Bonnell I. A., 2012, *MNRAS*, **424**, 2599
- Dale J. E., 2015, *New Astron. Rev.*, **68**, 1
- Dale J. E., Ercolano B., Bonnell I. A., 2012, *MNRAS*, **424**, 377
- Diaz-Miller R. I., Franco J., Shore S. N., 1998, *ApJ*, **501**, 192
- Draine B. T., 2011, *ApJ*, **732**, 100
- Draine B. T., Bertoldi F., 1996, *ApJ*, **468**, 269
- Fall S. M., Krumholz M. R., Matzner C. D., 2010, *ApJ*, **710**, L142
- Forbes J. C., Krumholz M. R., Goldbaum N. J., Dekel A., 2016, *Nature*, **535**, 523
- Franco J., Tenorio-Tagle G., Bodenheimer P., 1990, *ApJ*, **349**, 126
- Fukui Y., Kawamura A., 2010, *ARA&A*, **48**, 547
- Gavagnin E., Bleuler A., Rosdahl J., Teyssier R., 2017, *MNRAS*, **472**, 4155
- Geen S., Hennebelle P., Tremblin P., Rosdahl J., 2015, *MNRAS*, **454**, 4484
- Geen S., Pellegrini E., Bieri R., Klessen R., 2019, arXiv e-prints, p. [arXiv:1906.05649](#)
- Gong M., Ostriker E. C., Kim C.-G., 2018, *ApJ*, **858**, 16
- Gorti U., Hollenbach D., 2002, *ApJ*, **573**, 215
- Grenier I. A., Kaufman Bernadó M. M., Romero G. E., 2005, *Ap&SS*, **297**, 109
- Habing H. J., 1968, *Bull. Astron. Inst. Netherlands*, **19**, 421
- Haid S., Walch S., Seifried D., Wünsch R., Dinnbier F., Naab T., 2019, *MNRAS*, **482**, 4062
- He C.-C., Ricotti M., Geen S., 2019, arXiv e-prints, p. [arXiv:1904.07889](#)
- Hollenbach D., McKee C. F., 1979, *ApJS*, **41**, 555
- Hollenbach D., McKee C. F., 1989, *ApJ*, **342**, 306
- Hollenbach D. J., Tielens A. G. G. M., 1999, *Reviews of Modern Physics*, **71**, 173
- Hosokawa T., 2007, *A&A*, **463**, 187
- Hosokawa T., Inutsuka S.-i., 2006, *ApJ*, **646**, 240
- Hosokawa T., Inutsuka S.-i., 2007, *ApJ*, **664**, 363

Howard C. S., Pudritz R. E., Harris W. E., 2016, *MNRAS*, **461**, 2953

Hu C.-Y., Naab T., Glover S. C. O., Walch S., Clark P. C., 2017, *MNRAS*, **471**, 2151

Inoue T., Inutsuka S.-i., 2008, *ApJ*, **687**, 303

Inoue T., Inutsuka S.-i., 2009, *ApJ*, **704**, 161

Inutsuka S.-i., Inoue T., Iwasaki K., Hosokawa T., 2015, *A&A*, **580**, A49

Ishiki S., Okamoto T., 2017, *MNRAS*, **466**, L123

Kennicutt R. C., Evans N. J., 2012, *ARA&A*, **50**, 531

Kim J.-G., Kim W.-T., Ostriker E. C., 2016, *ApJ*, **819**, 137

Kim J.-G., Kim W.-T., Ostriker E. C., Skinner M. A., 2017, *The Astrophysical Journal*, 851, 93

Kim J.-G., Kim W.-T., Ostriker E. C., 2018, *ApJ*, **859**, 68

Koyama H., Inutsuka S.-i., 2000, *ApJ*, **532**, 980

Kruijssen J. M. D., et al., 2019, *Nature*, **569**, 519

Krumholz M. R., Matzner C. D., 2009, *ApJ*, **703**, 1352

Krumholz M. R., Fumagalli M., da Silva R. L., Rendaahl T., Parra J., 2015, *MNRAS*, **452**, 1447

Krumholz M. R., McKee C. F., Bland -Hawthorn J., 2018, arXiv e-prints, p. [arXiv:1812.01615](https://arxiv.org/abs/1812.01615)

Langer W., 1976, *ApJ*, **206**, 699

Lee E. J., Miville-Deschênes M.-A., Murray N. W., 2016, *ApJ*, **833**, 229

Lopez L. A., Krumholz M. R., Bolatto A. D., Prochaska J. X., Ramirez-Ruiz E., Castro D., 2014, *ApJ*, **795**, 121

Matzner C. D., 2002, *ApJ*, **566**, 302

McKee C. F., Storey J. W. V., Watson D. M., Green S., 1982, *ApJ*, **259**, 647

McKee C. F., van Buren D., Lazareff B., 1984, *ApJ*, **278**, L115

Mellem G., Arthur S. J., Henney W. J., Iliev I. T., Shapiro P. R., 2006, *ApJ*, **647**, 397

Murray N., Quataert E., Thompson T. A., 2010, *ApJ*, **709**, 191

Naab T., Ostriker J. P., 2017, *ARA&A*, **55**, 59

Nakatani R., Yoshida N., 2018, arXiv e-prints, p. [arXiv:1811.00297](https://arxiv.org/abs/1811.00297)

Nelson R. P., Langer W. D., 1997, *ApJ*, **482**, 796

Nelson R. P., Langer W. D., 1999, *ApJ*, **524**, 923

Osterbrock D. E., 1989, *Sky & Telesc.*, **78**, 491

Peters T., et al., 2017, *MNRAS*, **466**, 3293

Pineda J. L., Langer W. D., Velusamy T., Goldsmith P. F., 2013, *A&A*, **554**, A103

Pineda J. L., Langer W. D., Goldsmith P. F., 2014, *A&A*, **570**, A121

Planck Collaboration et al., 2011, *A&A*, **536**, A21

Rahner D., Pellegrini E. W., Glover S. C. O., Klessen R. S., 2017, *MNRAS*, **470**, 4453

Rahner D., Pellegrini E. W., Glover S. C. O., Klessen R. S., 2019, *MNRAS*, **483**, 2547

Raskutti S., Ostriker E. C., Skinner M. A., 2016, *ApJ*, **829**, 130

Raskutti S., Ostriker E. C., Skinner M. A., 2017, *ApJ*, **850**, 112

Roger R. S., Dewdney P. E., 1992, *ApJ*, **385**, 536

Rogers H., Pittard J. M., 2013, *MNRAS*, **431**, 1337

Seifried D., Haid S., Walch S., Borchert E. M., Bisbas T. G., 2019, arXiv e-prints, p. [arXiv:1906.01015](https://arxiv.org/abs/1906.01015)

Smith R. J., Glover S. C. O., Klessen R. S., 2014, *MNRAS*, **445**, 2900

Spitzer L., 1978, *Physical processes in the interstellar medium*, doi:10.1002/9783527617722.

Tan J. C., Beltrán M. T., Caselli P., Fontani F., Fuente A., Krumholz M. R., McKee C. F., Stolte A., 2014, in Beuther H., Klessen R. S., Dullemond C. P., Henning T., eds, *Protostars and Planets VI*. p. 149 ([arXiv:1402.0919](https://arxiv.org/abs/1402.0919)), doi:10.2458/azu_uapress_9780816531240-ch007

Tenorio-Tagle G., 1979, *A&A*, **71**, 59

Thompson T. A., Krumholz M. R., 2016, *MNRAS*, **455**, 334

Tielens A. G. G. M., Hollenbach D., 1985, *ApJ*, **291**, 722

Vázquez-Semadeni E., Colín P., Gómez G. C., Ballesteros-Paredes J., Watson A. W., 2010, *ApJ*, **715**, 1302

Weaver R., McCray R., Castor J., Shapiro P., Moore R., 1977, *ApJ*, **218**, 377

Whitworth A., 1979, *MNRAS*, **186**, 59

Williams J. P., McKee C. F., 1997, *ApJ*, **476**, 166

Wolfire M. G., Hollenbach D., McKee C. F., Tielens A. G. G. M., Bakes E. L. O., 1995, *ApJ*, **443**, 152

Wolfire M. G., Hollenbach D., McKee C. F., 2010, *ApJ*, **716**, 1191

Yorke H. W., 1986, *ARA&A*, **24**, 49

van Dishoeck E. F., Black J. H., 1988, *ApJ*, **334**, 771

APPENDIX A: MASS-TO-LUMINOSITY RATIO

To calculate the mass-to-luminosity ratio Ξ for the EUV and FUV radiation from a newborn star cluster, we use the SLUG code, a publicly available spectral population synthesis code (Krumholz et al. 2015). We adopt the same settings as in Kim et al. (2016), i.e., with the IMF given by Chabrier (2003), spectral synthesis model Starburst99, and stellar evolution tracks based on the Genova library. We have ran 1000 simulations for each cluster mass bin logarithmically spaced by 0.2 dex in the range of $10^2 M_{\odot} \leq M_* \leq 10^5 M_{\odot}$. We assume that the maximum mass of the cluster member star is $100 M_{\odot}$. We evaluate the photon number luminosity \mathcal{L}_{EUV} and \mathcal{L}_{FUV} for the energy ranges of $h\nu > 13.6$ eV (EUV) and 6.0 eV $< h\nu < 13.6$ eV (FUV), respectively.

Fig. A1 presents Ξ_{EUV} (left panel) and Ξ_{FUV} (right panel) as functions of the cluster mass M_* . Each panel shows 10th to 90th percentile range with the blue shade and the median value with the blue circles connected by the solid line. We see that the EUV ratio Ξ_{EUV} rapidly decreases with decreasing the cluster mass; the values for $10^3 M_{\odot}$ are more than one order of magnitude smaller than those for $10^5 M_{\odot}$. By contrast, the FUV ratio Ξ_{FUV} only decreases by a factor of a few, at most, from $10^5 M_{\odot}$ to $10^3 M_{\odot}$. This is because, in comparison to the EUV cases, the less massive stars contribute more to the FUV radiation.

We fit the median value of Ξ_{EUV} and Ξ_{FUV} as the following analytic functions M_* :

$$\log \left(\frac{\Xi_{\text{EUV}}}{1s^{-1}M_{\odot}^{-1}} \right) = \frac{46.70\chi^6}{2.70 + \chi^6}, \quad (\text{A1})$$

$$\log \left(\frac{\Xi_{\text{FUV}}}{1s^{-1}M_{\odot}^{-1}} \right) = \frac{47.02\chi^6}{0.92 + \chi^6}, \quad (\text{A2})$$

where $\chi = \log(M_*/M_{\odot})$. We have used these formulae in our calculations presented in the main part.

This paper has been typeset from a $\text{\TeX}/\text{\LaTeX}$ file prepared by the author.

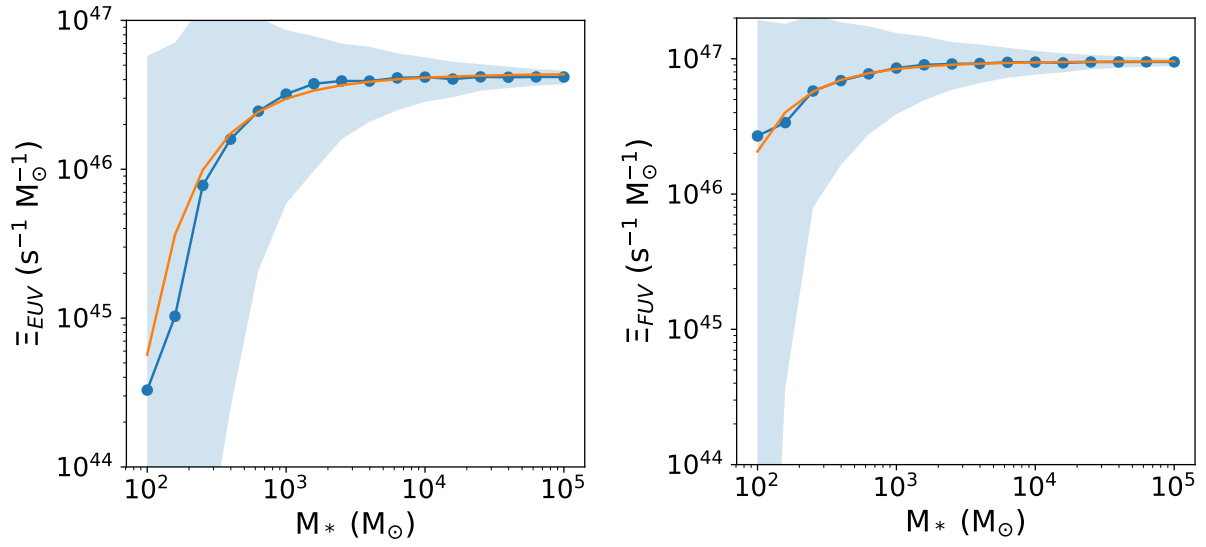


Figure A1. The ratio of EUV and FUV photons emitted per unit time to stellar mass $\Xi_{\text{EUV}} = S_{\text{EUV}}/M_*$ and $\Xi_{\text{FUV}} = S_{\text{FUV}}/M_*$. The blue line with circles represent the median value, while the shaded area represents the 10th to 90th percentile range from the simulation. Analytical fitting of the median value is showed with the orange line.